Modeling Hydraulic Response of Rock Fractures under Effective Normal Stress

Xupeng He, Marwah M. AlSinan, Dr. Hyung T. Kwak and Dr. Hussein Hoteit

Abstract /

The permeability of rock fractures and its variation with effective stress is of considerable interest in broad energy and environmental applications, such as enhanced oil and gas from hydrocarbon reservoirs, geothermal energy extraction, and geological carbon storage, among others. The permeability of a rock fracture is a complex function of various static parameters, including mechanical aperture, surface roughness, and fracture contact areas, all of which are the function of effective stress acting on the fracture walls.

The commonly used cubic law is unfit for most applications as it often overestimates the fracture permeability resulting in unreliable predictions. Several models are proposed in the literature with various levels of complexity and accuracy.

This work establishes a new comprehensive data-driven model to estimate the hydraulic properties of rock fractures as a function of the fracture static characteristics and dynamic effective stress. A data set measuring fracture permeability in terms of confining stress, fluid pressure, and other rock parameters is compiled to identify the potential trends. We further verify the proposed model with coupled flow geomechanic simulations. The results show that the potential trends observed from the data set match with the theoretical model.

We show that our proposed model is superior to all the models that we tested from the literature. The coupled workflow offers an efficient approach to characterize the hydraulic response of rock fractures under effective stress. The proposed model is simple, accurate, and efficient, and therefore can be implemented to capture stress dependent permeability of fracture networks in field-scale reservoir simulations.

Introduction

Accurate modeling of single and multiphase fluid flow through fractured porous media requires a fundamental understanding of the stress dependent hydraulic behaviors of rock fractures[1, 2].

The permeability of a rock fracture is a complex function of various static and dynamic parameters, including the fracture mechanical aperture, surface roughness, and fracture contact areas, which are subject to alterations by the stress field acting on the fracture walls. Characterizing the relationship between fracture permeability and effective stress has been extensively investigated in the literature. Table 1[5-16] is a review listing 12 empirical and theoretical models, commonly used. These models, however, exhibit various limitations related to the level of complexity, accuracy, and general applicability.

In this study, a new comprehensive model that quantifies the relationship between fracture permeability and effective normal stress is proposed. We first derive a theoretical model based on a modified cubic law, which incorporates the effect of fracture hydraulic aperture, mechanical aperture, roughness, and contact area.

To validate the model, we collected a database of experimental data from the literature, reporting fracture permeability in terms of pore pressure, confining stress, and other rock properties such as Young's modulus, Poisson's ratio, and uniaxial compressive strength. The fracture permeability database includes both natural and synthetic fractures with different rock types corresponding to siltstone, sandstone, shale, and carbonate. The subsequent analysis seeks to identify potential correlations in the observed data and to develop a data-driven representative model. We further verify the developed model using coupled flow geomechanics simulations. Fluid flow in the fracture is described by high-resolution full physics Navier-Stokes equations[3], and the geomechanical deformation is quantified through the elastic contact theory[4].

We will first review the concepts of existing models, and then present a detailed derivation of the proposed model. We then show the data set, compiled from published experimental data, relating fracture permeabilities and effective normal stress. We also compare the proposed model with existing models in the literature. Finally, we will demonstrate the model performance with coupled flow geomechanics simulations.

Table 1 *A review listing the 12 empirical and theoretical models commonly used.*

Reference	Model	Category	Highlights
Snow (1968)[5]	$k = k_0 + Mw^2/S\left(\sigma_e - \sigma_{e,0}\right)$	Theoretical	Assumes w is independent of effective stress.
Louis (1969)[6]	$k = k_0 \exp\left(-\alpha\sigma_e\right)$	Empirical	Based on well pumping test at different depths.
Jones (1975)[7]	$k = k_0\left[\log\left(\frac{\sigma_{e,k=0}}{\sigma_e}\right)\right]^3$	Empirical	Fitted with data from carbonate rock fractures.
Nelson (1975)[8]	$k = A + B\sigma_e^{-n}$	Empirical	Fitted with data from fractured sandstone.
Gangi (1978)[9]	$k = k_0\left[1-\left(P/P_1\right)^m\right]^3$	Theoretical	Assumes power-law distribution of asperities.
Kranz et al. (1979)[10]	$k = \frac{k_0 A_0}{A}\left(\sigma_c - p_p\right)^{-n}$	Empirical	Fitted with data from jointed Barre granite.
Walsh (1981)[11]	$k = k_0\left[1-\sqrt{2}\frac{h}{a_0}\ln\left(\frac{\sigma_e}{\sigma_{e,0}}\right)\right]^3$	Theoretical	Assumes circular contact area.
Gale (1982)[12]	$k = B\sigma_e^{\alpha}$	Theoretical	Based on the parallel plate.
Seidle et al. (1992)[13]	$k = k_0 e^{-3c_f\left(\sigma_e - \sigma_{e,0}\right)}$	Theoretical	Design for coal; c_f – constant.
Li et al. (2013)[14]	$k = k_0 e^{-3\overline{c_f}\left(\sigma_e - \sigma_{e,0}\right)}$ $\overline{c_p} = \frac{a}{\sigma_e - \sigma_{e,0}}\ln\left(\frac{\sigma_e + b}{\sigma_{e,0} + b}\right)$	Theoretical	Negligible difference between c_f and c_p.
Chen et al. (2015)[15]	$k = k_0 e^{-3\overline{c_f}\left(\sigma_e - \sigma_{e,0}\right)}$ $\overline{c_f} = c_{f,0}\frac{1-e^{-\alpha\left(\sigma_e - \sigma_{e,0}\right)}}{\alpha\left(\sigma_e - \sigma_{e,0}\right)}$	Semi-Empirical	Design for shale rock fractures; stress dependent. c_f
Zhou et al. (2019)[16]	$k = k_0\left(1+\frac{B}{p_p}\right)e^{-3\overline{c_f}\left(\sigma_e - \sigma_{e,0}\right)}$	Theoretical	Consider the gas slippage effect.

Theoretical Analysis

Geometric Characteristics of Rock Fractures

Subsurface rock fractures are formed of surfaces with anisotropic roughness, varying aperture, and contact areas of fracture walls, Fig. 1. The geometric fracture characteristics are crucial for understanding the hydro-mechanical behaviors of rock fractures. Therefore, the following parameters are considered in the proposed model.

Mechanical aperture. The mechanical aperture, a, representing the average aperture of the whole void (open) areas, including the isolated void areas, is given by:

$$a = \frac{\sum_{i=1}^{Nv} a_i}{N} \quad 1$$

where, N_v and N are the numbers of grid points within the isolated void areas, and within the whole fracture area, respectively.

Contact area. The asperity contact areas serves as the bridge connecting the fluid flow and geomechanics deformation. The existence of contact areas (Fig. 1a), which represent the primary resistance to the confining stress applied on the fracture, controls the main mechanical deformation and the tortuous flow behaviors of fluid flow.

Contact areas may introduce a significant effect on the flow, e.g., some isolated void areas, Fig. 1b, have no contribution to fluid flow, which should be accounted for. In this study, contact areas, including isolated void areas and its effect on fluid flow, are quantitatively characterized by the contact ratio, c, Eqn. 2:

$$c = \frac{N_c + N_i}{N} \quad 2$$

where N_c and N_i are the numbers of grid points within the contact and isolated void areas, respectively.

Fracture roughness. The roughness introduces resistance to flow, resulting in lowering the fracture hydraulic aperture. In this study, we use the joint roughness coefficient (JRC) to quantify the fracture surface roughness[17].

Fig. 1 *The geometric characteristics of rock fractures. (a) The aperture field of 3D rough fracture showing the contact area and isolated void area (exaggerated area a). (b) The exaggerated 2D rough fracture showing anisotropic roughness, varying aperture, and asperity contact on two mating surfaces.*

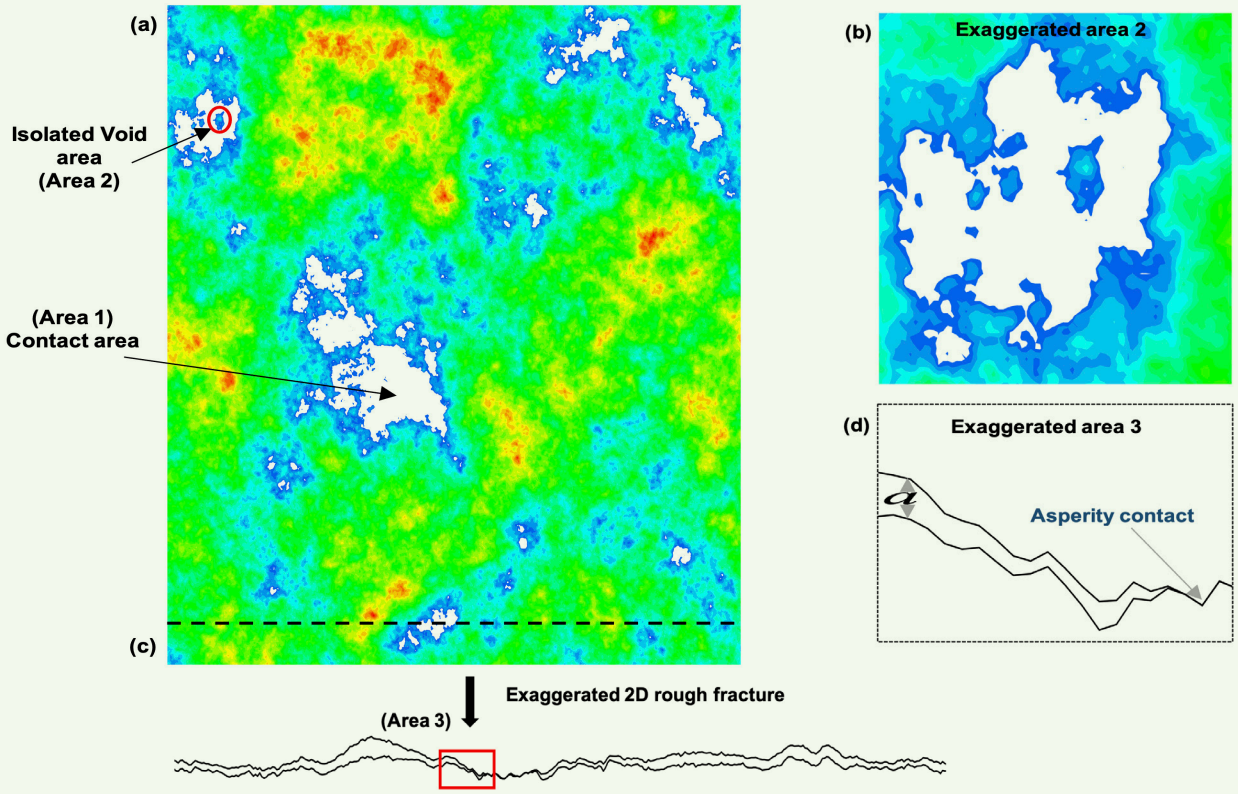

$$JRC = 51.16\left(Z_2\right)^{0.531} - 11.44 \quad (3)$$

where Z_2 is the root mean square (RMS) of first derivation value.

Fracture relative roughness, (a/ε) defined as the ratio of mechanical aperture to the standard deviation of the fracture aperture, is used to describe the degree that the surface asperities protrude into the fluid[18].

Model Development

The Walsh model (1981)[11] has been widely used to characterize the stress dependent hydraulic behavior of rock fractures. Consequently, this model assumes circular contact areas and neglects changes in fracture roughness resulting from normal stress. The permeability model proposed is given by:

$$k = \frac{1-c}{1+c}\frac{2a^3}{3\mu} \quad (4)$$

where k is the fracture permeability.

We modify Eqn. 4 by introducing correction terms for fracture roughness and an irregular shape contact area. We apply a correction term for the irregular shape contact area[19] and introduce the friction factor, f, to account for the effect of fracture roughness. Therefore, the proposed flow model becomes:

$$k = \frac{1-\beta c}{1+\beta c}\frac{1}{f}\frac{2a^3}{3\mu} \quad (5)$$

where $\beta = (1+\alpha)^2/4\alpha$, with α as the equivalent aspect ratio of the ellipse, which can be chosen by imaging the actual asperities to be replaced by an equal number of ellipses with the same total area and perimeter.

Changing the normal stress, σ_n, on the fracture may alter a, c, and the fracture roughness. Therefore, the geometric parameters mentioned here are functions of the normal stress[11, 20]. Differentiating Eqn. 5 with respect to normal stress and rearranging gives us:

$$\frac{d\ln k}{d\sigma_n} = -\frac{2\beta}{1-\beta^2c^2}\left(\frac{dc}{d\sigma_n}\right) - \frac{1}{f}\left(\frac{df}{d\sigma_n}\right) + \frac{3}{a}\left(\frac{da}{d\sigma_n}\right) \quad (6)$$

For a fracture surface with random surface topography, Walsh and Grosenbaugh (1979)[21] showed that the change, da, in the aperture resulting from a change, $d\sigma_n$, in normal stress, is written as:

$$da/d\sigma_n = -\sqrt{2}\,\varepsilon/\sigma_n \quad (7)$$

where ε is the RMS of the height distribution.

Integrating Eqn. 7 yields:

$$a = -\sqrt{2}\varepsilon \bullet \ln\left(\sigma_n\right) + C_1 \quad (8)$$

Following Greenwood and Williamson (1966)[22] and Whitehouse and Archard (1970)[23], we find the relationship between the contact area and normal stress, which exhibits a linear trend for this model is:

$$dc/d\sigma_n = b = \sqrt{3}\,\pi(\lambda/\varepsilon)\left(1-\nu^2\right)/E \quad (9)$$

where E and v are Young's modulus and Poisson's ratio, respectively, andis λ the auto-correction distance.

Integrating Eqn. 9 yields:

$$c = b \bullet \sigma_n + C_2 \quad (10)$$

Huo and Benson (2015)[20] found that the friction factor has an exponential relationship with normal stress, as:

$$f = m \bullet e^{n\sigma_n} + f_i \quad (11)$$

where f_i is the irreducible friction factor.

Differentiating Eqn. 11 gives us:

$$df/d\sigma_n = mn \bullet e^{n\sigma_n} \quad (12)$$

Substituting Eqn. 7, Eqn. 9, and Eqn. 12 into Eqn. 6, and rearranging them gives us:

$$d\ln k = -\frac{2\beta b}{1-\beta^2 c^2}d\sigma_n - \frac{mn}{f}e^{n\sigma_n}d\sigma_n + 3\sqrt{2}\frac{\varepsilon}{a}\frac{d\sigma_n}{\sigma_n} \quad (13)$$

Integrating Eqn. 13 from $\sigma_{n,0}$ to σ_n yields the first term of Eqn. 13:

$$\int_{\ln k_0}^{\ln k} d\ln k = \ln\frac{k}{k_0} \quad (14)$$

and integrating the second term of Eqn. 13:

$$-\int_{\sigma_{n,0}}^{\sigma_n}\frac{2\beta b}{1-\beta^2 c^2}d\sigma_n = \left[\ln\frac{1-\beta c}{1+\beta c}\right]_{\sigma_{n,0}}^{\sigma_n} = \ln\left(\frac{1-\beta c}{1+\beta c}\bullet\frac{1+\beta c_0}{1-\beta c_0}\right) \quad (15)$$

Introducing Eqn. 10 into Eqn. 15 gives:

$$-\int_{\sigma_{n,0}}^{\sigma_n}\frac{2\beta b}{1-\beta^2 c^2}d\sigma_n = \ln\left[\frac{1-B\left(\sigma_n-\sigma_{n,0}\right)}{1+C\left(\sigma_n-\sigma_{n,0}\right)}\right] \quad (16)$$

where $B = \beta b/\left(1-\beta c_0\right)$ and $C = \beta b/\left(1+\beta c_0\right)$.

Similarly, integrating the third term of Eqn. 13:

$$-\int_{\sigma_{n,0}}^{\sigma_n}\frac{mn}{f}e^{n\sigma_n}d\sigma_n = -\left[\ln f\right]_{\sigma_{n,0}}^{\sigma_n}$$
$$= -\ln\left(1+\left[1-f_i/f_0\right]\left[\exp n\left(\sigma_n-\sigma_{n,0}\right)-1\right]\right) \quad (17)$$

and integrating the fourth term of Eqn. 13:

$$\int_{\sigma_{n,0}}^{\sigma_n} 3\sqrt{2}\frac{\varepsilon}{a}\frac{d\sigma_n}{\sigma_n} = \left[\ln a^3\right]_{\sigma_{n,0}}^{\sigma_n} = \ln\left(1-\frac{\sqrt{2}\varepsilon}{a_0}\ln\frac{\sigma_n}{\sigma_{n,0}}\right)^3 \quad (18)$$

Combining Eqn. 14, Eqn. 16, Eqn. 17, and Eqn. 18:

$$\frac{k}{k_0} = \left(1-\frac{\sqrt{2}\varepsilon}{a_0}\ln\frac{\sigma_n}{\sigma_{n,0}}\right)^3\left[\frac{1-B\left(\sigma_n-\sigma_{n,0}\right)}{1+C\left(\sigma_n-\sigma_{n,0}\right)}\right]$$
$$\frac{1}{1+\left[1-f_i/f_0\right]\left[\exp n\left(\sigma_n-\sigma_{n,0}\right)-1\right]} \quad (19)$$

where k_0, a_0, and f_0 are the fracture permeability, aperture, and friction factor at initial normal stress $\sigma_{n,0}$, respectively. We can observe that the Walsh model is a special case of Eqn. 19 when $\beta = 1$ and $f_i = f_0$. Note that all factors that influence the fluid flow through the rock fractures are represented in Eqn. 19. The first, second, and third terms in the right-hand side represent the effect of fracture aperture, tortuosity (caused by contact area), and fracture roughness, respectively.

The effect of change in the pore pressure, change in applied stress, or change in both the pore pressure and applied stress can be described by the concept of effective stress, which is given as[24]:

$$\sigma_{n,e} = \sigma_n - \alpha P_p \quad (20)$$

where $\sigma_{n,e}$, P_p, and a are the effective normal stress, fluid pore pressure, and the effective stress coefficient, respectively. Note that a cannot always be 1, as some models suggest. Experimental data[10] showed that a is approximately 0.9 for fractures with a polished surface and about 0.56 for tension fracture from Barre granite. The study regarding the effective stress coefficient estimation will be addressed in separate work.

Once all needed parameters in Eqn. 19 and Eqn. 20 are measured for a specific fracture, we can quantitatively characterize its stress dependent hydraulic behavior responding to the applied effective normal stress. Equation 19 captures the effect of three parameters: fracture aperture, tortuosity, and fracture roughness. The expression of fracture aperture is of the third power, thereby magnifying any small changes, whereas the tortuosity and fracture roughness show less influence. Consequently, the effect of tortuosity and roughness could be neglected when applying relatively low effective stress. Accordingly, if we consider the assumption under low effective stress, Eqn. 19 is written in the following compact form:

$$\left(k/k_0\right)^{1/3} = 1-\left(\sqrt{2}\varepsilon/a_0\right)\ln\left(\sigma_{n,e}/\sigma_{n,e,0}\right) \quad (21)$$

Data Compilation

We verify the validity of Eqn. 19 with experimental data, compiled from the literature. To verify Eqn. 19, the parameters, including confining pressure, pore pressure, effective stress coefficient, and other rock properties such as Young's modulus, Poisson's ratio, the RMS of the height distribution, contact area distribution, and irreducible friction factor, should be measured. Subsequently, the related flow and rock properties in Eqn. 19 cannot be obtained entirely from the literature, which makes it infeasible for testing Eqn. 19. Instead, assessing the validity of Eqn. 21 can indicate the validity of Eqn. 19 within a specific range of low effective stress. We observe in Eqn. 21 that the cube root of the fracture permeability varies linearly with $\ln(\sigma_{n,e})$.

To verify the potential linear trends, we collected a data set relating fracture permeability in terms of confining stress, pore pressure, and other rock properties from published experimental sources. The data set spans about 10 orders of magnitude in permeability variations and includes both natural and artificial fractures with different rock types corresponding to siltstone, sandstone, carbonate, and shale. The data set is plotted in $(k/k_0)^{1/3}$-$\ln(\sigma_{n,e}/\sigma_{n,e,0})$ scale combinations.

We identified trends in the observed data to develop a data-driven representative model. We note that the data set exhibits a prevalent negatively linear trend in the $(k/k_0)^{1/3}$-ln($\sigma_{n,e}/\sigma_{n,e,0}$) space, Fig. 2. This shows a good match with the theoretical model with an averaged R^2 value of about 0.97.

As observed in Fig. 2, the linear trend fits well with the observed data with the range of low stress. As discussed, the effect of aperture exhibits a significant contribution to the change in fracture permeability within the low stress area, which is consistent with Eqn. 21. We observe that in the high stress conditions (black circle in Fig. 2), the linear trend is not honored, which indicates the potential effect of tortuosity and fracture roughness. With the increasing applied stress, more asperities are coming into contact, creating a more tortuous flow behavior. On the other hand, the fracture's relative roughness becomes more prominent as the fracture surfaces come closer with increasing applied stress.

In summary, the linear trend fits well within the limited range of stress conditions. The linear trend is violated when the effect of tortuosity and roughness becomes pronounced, with the increasing applied stress. Few studies regarding stress dependent fracture permeability under high stress have been investigated in the literature. We will address the contribution of aperture, tortuosity, and roughness to fracture permeability change in future work.

We demonstrate the performance of the proposed model with existing models from the literature. Except for the logarithmic-type relationship, we categorize other existing models from Table 1 into three main types: exponential-type models[6, 13-16], power-type models[8, 10, 12], and reciprocal model[5]. Note that we assume the fracture compressibility in the exponential-type models is independent of stress.

Exponential Type

The general normalized form for the exponential-type relationship is given by:

$$(k/k_0) = A\exp\alpha\left(\sigma_{n,e}/\sigma_{n,e,0}\right) \quad (22)$$

For the convenience of visualizing all the data, we plot the data set in all ln(k/k_0)-ln($\sigma_{n,e}/\sigma_{n,e,0}$)-ln($\sigma_{n,e}/\sigma_{n,e,0}$) scale combinations, Fig. 3. The average $R^2 = 0.86$.

Power Type

The general normalized form of the power-type relationship is given by:

$$(k/k_0) = A\left(\sigma_{n,e}/\sigma_{n,e,0}\right)^{\alpha} \quad (23)$$

Taking the logarithm of Eqn. 23 yields:

$$\ln(k/k_0) = \alpha\ln\left(\sigma_{n,e}/\sigma_{n,e,0}\right) + B \quad (24)$$

The data set is plotted in all ln(k/k_0)-ln($\sigma_{n,e}/\sigma_{n,e,0}$)-ln($\sigma_{n,e}/\sigma_{n,e,0}$) scale combinations, Fig. 4. The average $R^2 = 0.955$.

Reciprocal Type

The general normalized form for the reciprocal-type relationship is given by:

$$(k/k_0) = A + B/\left(\sigma_{n,e}/\sigma_{n,e,0}\right) \quad (25)$$

where we plot the data set in all ln(k/k_0)-ln($\sigma_{n,e}/\sigma_{n,e,0}$)-ln($\sigma_{n,e}/\sigma_{n,e,0}$) scale combinations, Fig. 5. The average $R^2 = 0.91$.

Fig. 2 *The cube root of a normalized fracture permeability vs. the normalized effective stress. The data was gathered from shale (circle), carbonate (triangle), and sandstone (square). Data set: 311 data points from 21 fractured cores.*

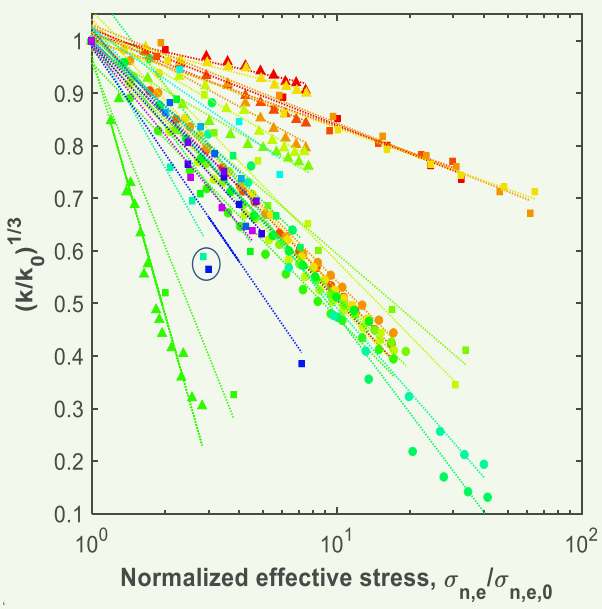

Fig. 3 *The normalized fracture permeability vs. the normalized effective stress. The data was gathered from shale (circle), carbonate (triangle), and sandstone (square). Data set: 311 data points from 21 fractured cores.*

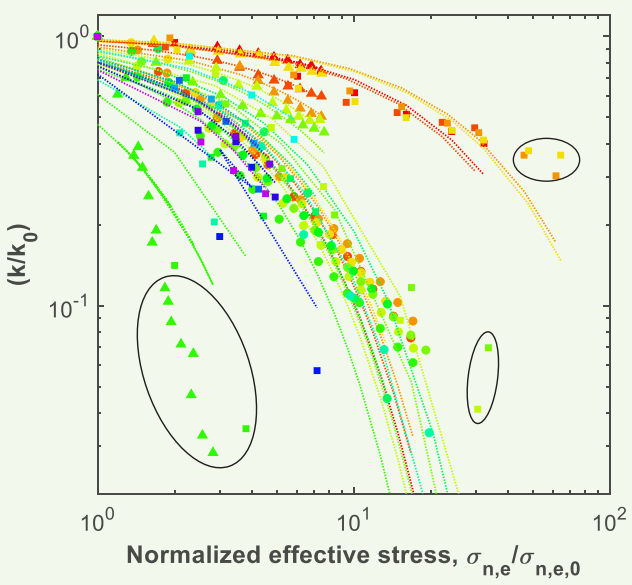

Fig. 4 *The normalized fracture permeability vs. the normalized effective stress. The data was gathered from shale (circle), carbonate (triangle), and sandstone (square). Data set: 311 data points from 21 fractured cores.*

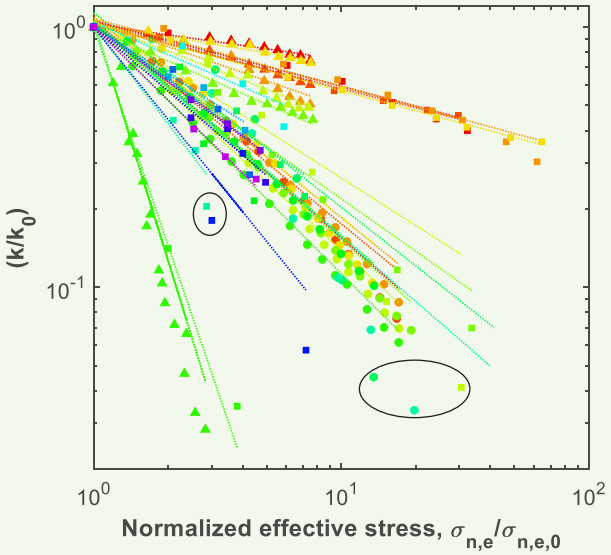

Fig. 5 *The normalized fracture permeability vs. the normalized effective stress. The data was gathered from shale (circle), carbonate (triangle), and sandstone (square). Data set: 311 data points from 21 fractured cores.*

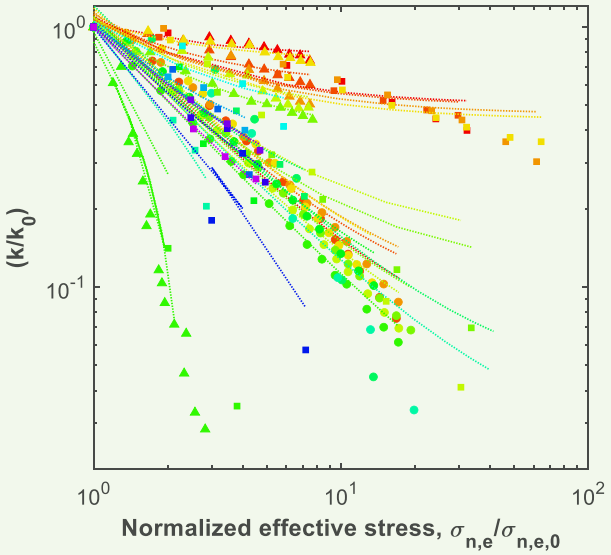

We can see in Figs. 3, 4, and 5 that the scatter points, which deviate from the corresponding fitted trend within some areas (see black circles in corresponding figures), correspond to the exponential-, power- and reciprocal-types. These models perform poorly for specific rock types within specific stress conditions.

Table 2 summarizes these observations, showing the R^2 value based on the curve fitting with the observed data for the model types. Based on the data set matching, the proposed model shows the best match for the observed data with an average R^2 of 0.971, followed by the power-type, exponential and reciprocal models with an R^2 of 0.955, 0.944, and 0.913, respectively. Moreover, the proposed model shows the most stable prediction with the standard deviation of R^2 (σ_{R^2}) is approximately 0.029, which is the lowest among all models.

In terms of specific rock types, the proposed model presents the best match for fractured shale rocks, whereas a less accurate match was observed for fractured carbonate rocks. More data sets need to be collected to confirm this observation. The mismatch for carbonates may result from high effective stress, where the effect of tortuosity and roughness becomes essential.

We will review the data set and find the effective stress applied on Barre granite[10], reaching up to 160 MPa — the highest in the data set. The other possible reason is that the calculation of the effective stress. Most publications in the literature just take α to be 1 for simplifying the effective stress calculation. As previously mentioned, measurements of flow through granite rock fractures with different roughness[10] showed that α can vary between 0.5 and 1.0, which has a significant effect, especially for cases with high fluid pressure. We observed in Table 2 that all models, except for the exponential model, show a less accurate match between the corresponding trend and the observed data on carbonate rocks. This could

Table 2 *The R^2 value of the curve fitting for our model types.*

Model R^2	Proposed Model	Exponential Type	Power Type	Reciprocal Type
Shale	0.992	0.935	0.974	0.956
Carbonate	0.955	0.872	0.947	0.853
Sandstone	0.965	0.807	0.966	0.913
$\overline{R^2}$	0.971	0.858	0.955	0.913
σ_{R^2}	0.029	0.113	0.034	0.076

be related to the temperature effect in the experimental data[25], where the same granite rock was used under different temperatures. These results require further investigation.

Flow Geomechanics Simulation

Mathematical Formulation

We further demonstrate the proposed model using coupled flow geomechanics simulations. Figure 6 shows the flow chart of the coupling flow geomechanics algorithm. The coupling algorithm operates sequentially in the following three steps with detailed descriptions.

Geomechanical Deformation of Rock Fractures

The main parameters in Fig. 7 shows the unmated rough fracture surfaces sliced from the 3D rock fractures, describing definitions of surface height (a), and composite topography (b).

The contact theory of two rough surfaces (both mated and unmated) proposed[4] gives the fracture closure values under different normal stresses. Combining with Eqn. 20, the contact theory gives:

$$\sigma_{n,e} = \frac{4}{3}\eta\langle\psi\rangle\langle E'\rangle\langle\beta^{1/2}\rangle\int_{d_0-\delta}^{\infty}(z-d_0+\delta)^{3/2}\phi(z)dz \qquad 26$$

where $\sigma_{n,e}$ is the effective normal stress, as input; δ is the fracture closure displacement, as output; η is the total number of local maxima per unit area; $\langle\psi\rangle$ is the mean of tangential stress correction factor $\langle E'\rangle$ is the mean of elastic constant; $\langle\beta^{1/2}\rangle$ is the mean of square root of curvature term; z is the height of local maximum in Fig. 7b; d_0 is the distance between reference planes at $\sigma_{n,e}=0$, and $\phi=(z)$ is the probability density function.

Once all needed statistical and rock parameters in Eqn. 27 are measured, the relation between $\sigma_{n,e}$ and δ can be established, Fig. 6b. Given any effective normal stress (input), the output δ can be obtained. The new 3D topography of rock fracture is then constructed by subtracting the fracture closure displacement value, δ, from the initial 3D topography of the rock fracture. Here, we show the aperture distributions of 3D rock fracture before and after the applied normal stress, Figs. 6a and 6c.

Fluid Flow in Rock Fractures

The Navier-Stokes is theoretically considered the most accurate approach for analyzing the hydraulic properties of rock fractures[3, 26]. We calculate the flow rate, Q, after applying the high-resolution Navier-Stokes equations to the newly constructed 3D rock fractures. Parallel

Fig. 6 *A flowchart of the proposed coupling flow geomechanics algorithm. (a) The initial aperture field, (b) The relationship between the fracture closure and the effective normal stress, obtained from Eqn. 27, (c) The newly updated aperture field after applying specific effective normal stress, and (d) The boundary conditions applied in the NS simulation and describes the normalized velocity distribution within the newly updated rock fractures. The algorithm iterates with the above steps in a loop.*

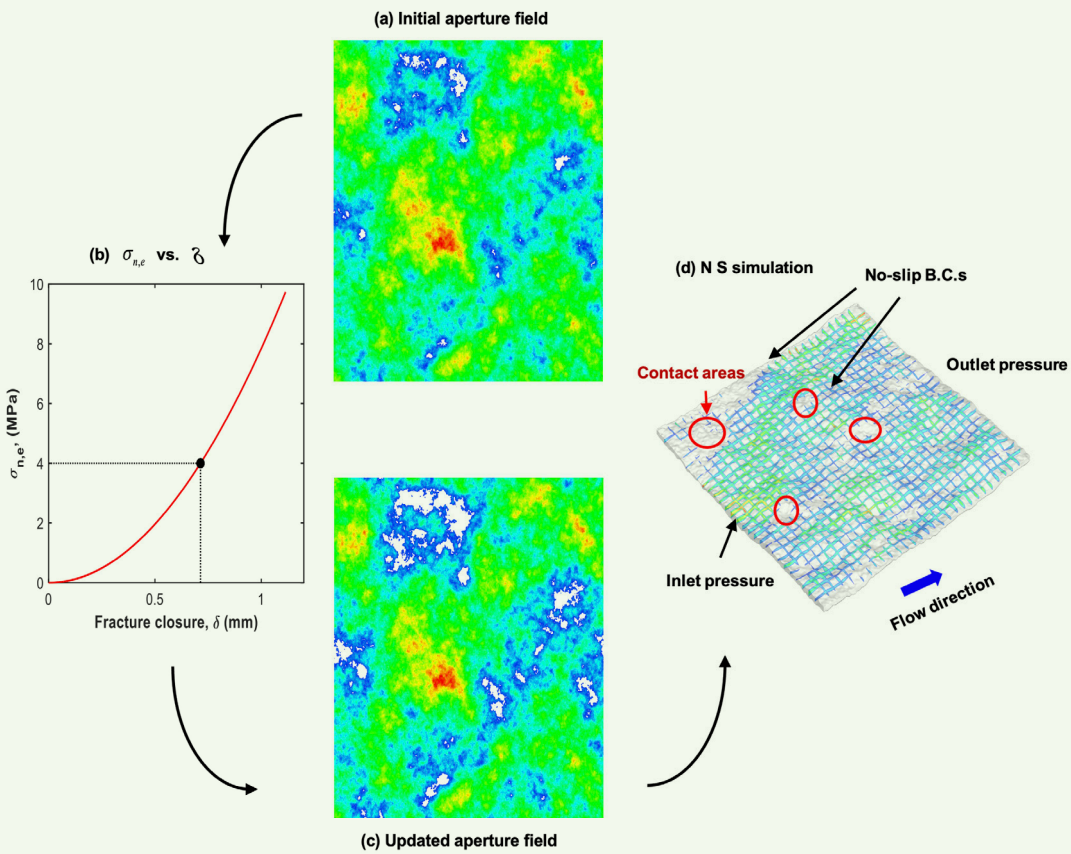

Fig. 7 *(a) A cross-section of 3D rock fractures showing two unmated rough fracture surfaces. The surface heights are measured from the parallel reference planes. (b) The composite topography, defined as the sum of the upper and lower surface heights. Note that the local maximum (red circle in (b)) reflects the local minimum aperture (red circle in (a)), where asperity contact will form.*

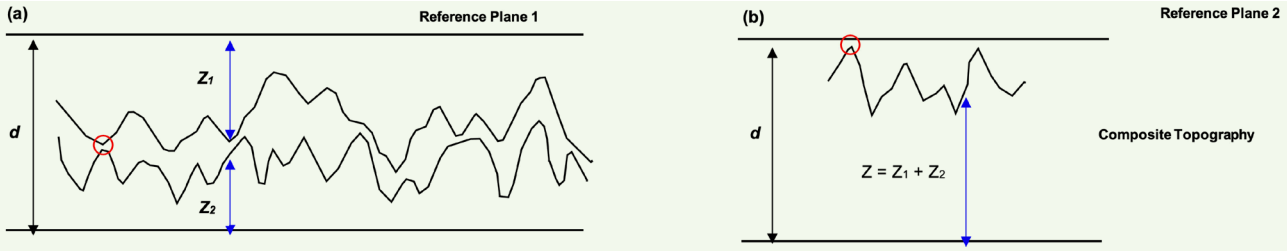

computing techniques enabled us to perform high-resolution simulations for hundreds of fracture cases, which are used to verify the developed coupling algorithm and proposed model under various lab and field conditions.

Fracture Permeability Calculation

Finally, the fracture permeability is back calculated based on Darcy's law and Cubic law.

$$a_h = \left(\frac{12Q\mu}{w\nabla P}\right)^{1/3} \quad 27$$

Then, from the Cubic law:

$$k = \frac{a_h^2}{12} = (12)^{1/3}\left(\frac{Q\mu}{w\nabla P}\right)^{2/3} \quad 28$$

where a_h is the hydraulic aperture, μ is the dynamic viscosity, w is fracture width, p is the pressure, and k is the fracture permeability.

The coupling algorithm sequentially iterates the above three steps until the final state of effective stress is reached. We plot all data pairs of $\sigma_{n,e}$ and k to identify the match between the potential trend observed from the data and the proposed model.

Simulation Example

We demonstrate the proposed coupling algorithm and verify the performance of the developed model with a 3D rough rock fracture. We assume no shearing effect during the compression process. All fractures share the same size — both the width and length of 100 mm with the same resolution of approximately 0.1 mm.

Figure 8 shows the probability density function of the aperture field under the increasing effective normal stress, labeled as S1, S2, S3, and S4, respectively. As observed in Fig. 8, the peak of the pdf curve shifts toward the left with the increasing effective normal stress.

Figure 9 shows the evolution of the contact area within the aperture field with an increasing effective normal stress corresponding to 0.1 MPa, 2.4 MPa, 3.8 MPa, and 6.4 MPa. We observe the existence of isolated void areas, which should be included in the effective contact areas.

Table 3 summarizes the geometrical fracture parameters with the increasing effective normal stress. We observe that in Table 3, the mean aperture decreases with the increasing effective normal stress, whereas c shows the reverse trend, as expected. The standard deviation

Fig. 8 *The probability density function of the aperture field with an increasing normal stress. The lefthand side of the figure reflects the existence of the contact area.*

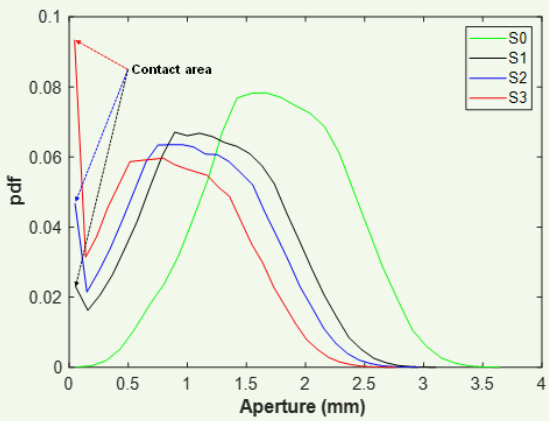

Fig. 9 *The evolution of the contact area with an increasing effective normal stress corresponding to 0.1 MPa, 2.4 MPa, 3.8 MPa, and 6.4 MPa.*

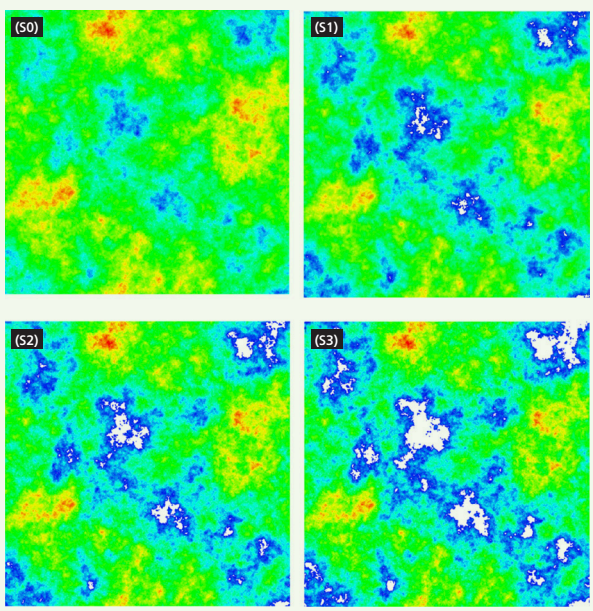

Table 3 *The fracture geometry statistics parameters under $\sigma_{n,e}$. These parameters are mean aperture, aperture standard deviation, fracture surface roughness, fracture relative roughness, and contact ratio, respectively.*

Parameters	S0	S1	S2	S3
$\langle a \rangle$ (mm)	1.75	1.20	1.06	0.87
σ_a (mm)	0.56	0.56	0.55	0.54
JRC (-)	19.47	19.46	19.44	19.43
$\sigma_a / \langle a \rangle$ (-)	3.12	2.15	1.91	1.62
c (%)	Points of Contact	1.26	3.12	7.08

of the aperture field and the fracture surface roughness are almost unaltered, as we apply the moving down of the top fracture surface to mimic the compression process. Consequently, the fracture relative roughness increases significantly as the fracture aperture reduces.

Following these steps, we apply the Navier-Stokes equations and calculate the corresponding fracture permeability under corresponding effective normal stress. We plot the data pair of $\sigma_{n,e}$ and k to seek the potential trend, Fig. 10.

Figure 10 shows a good match between the simulation results and the proposed model. The simulation results not only demonstrate the validity of the proposed model, but also show the potential of the proposed coupling algorithm. The coupling algorithm offers an efficient method for quantifying the stress dependent hydraulic behaviors of rock fractures, which significantly reduce the computational cost with good accuracy.

We will test the generality of the proposed coupling algorithm and the developed model using more rock fractures in future work. We will also demonstrate the superiority of the proposed model with existing models in the literature.

Fig. 10 *The cube root of the fracture permeability vs. the effective normal stress with different models.*

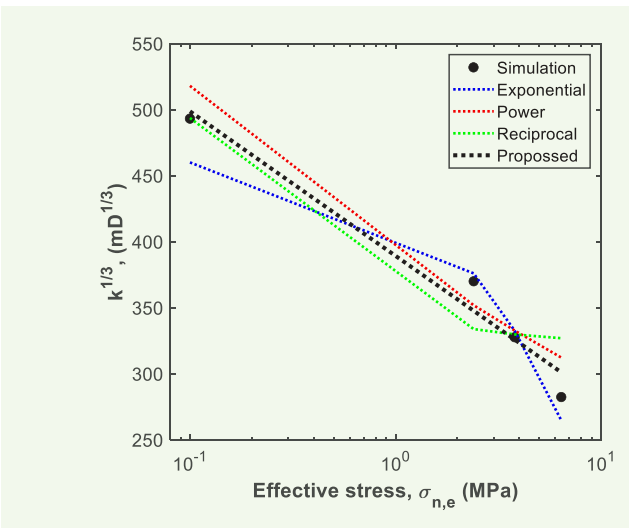

Conclusions

This work investigates the stress dependent hydraulic behaviors of rock fractures from theoretical, experimental data, and numerical perspectives. The main observations from this study include:

- This work introduces a new comprehensive data-driven model, which is a generalization of the model by Walsh (1981)[11]. This model, describing the relation between fracture permeability and effective normal stress, incorporates the effect of fracture aperture, tortuosity, and roughness. The sensitivity of fracture permeability to change in the aperture is higher than tortuosity and roughness, as the expression for aperture gives third power, whereas tortuosity and roughness are not.
- This work compiles a data set relating fracture permeability and effective stress. The data set integrates measurements within 10 orders of magnitude in fracture permeability, including natural/artificial fractures with different rock types (siltstone, sandstone, carbonate, and shale).
- The data exhibits a prevalent negatively linear trend on the $(k/k_0)^{1/3}$-$\ln(\sigma_{n,e}/\sigma_{n,e,0})$ space, which shows a good match with our proposed model. The linear trend is violated with the increasing applied stress, showing that the effect of tortuosity and roughness becomes essential. This is caused by a combination of two concurrent phenomena: more asperity contacts create more tortuous flow behavior, and the fracture surfaces come closer, resulting in more significant relative roughness.
- The work presents a review listing 12 models from the literature, which are mainly categorized into three types: exponential-type, power-type, and reciprocal-type. We show that our proposed model is superior to other models.
- The coupled flow geomechanics algorithm offers an efficient approach for quantifying stress dependent hydraulic behaviors of rock fractures, in which fluid flow through rock fractures is described using the Navier-Stokes equations, and fracture closure or

opening displacement is quantified using the elastic contact theory. The potential trend observed from the simulation results shows a good match with the theoretical model.

- The proposed model is comprehensive, accurate, and efficient; therefore, it can be implemented to capture the pressure dependent permeability of fractured media in field-scale simulations.

Future work will be focused on: (1) stress dependent permeability of rock fractures under high effective stress as well as the relative contribution of aperture, tortuosity, and roughness to the permeability change, (2) study of the effective stress coefficient, and (3) collecting more experimental data for fracture permeability and effective stress, especially for cases with high effective stress.

Acknowledgments

This article was prepared for presentation at the ARMA/DGS/SEG International Geomechanics Symposium, al-Khobar, Saudi Arabia, November 3-5, 2020.

The authors would like to thank Saudi Aramco for funding this research. We would also like to thank King Abdullah University of Science and Technology (KAUST) for the support and for providing licenses of MATLAB, COMSOL, and Ansys.

References

1. Grant, M.A. and Bixley, P.F.: *Geothermal Reservoir Engineering*, 2nd edition, Academic Press, 2011, 378 p.
2. Nelson, R.A.: *Geologic Analysis of Naturally Fractured Reservoirs*, 2nd edition, Elsevier, 2001, 352 p.
3. Brush, D.J. and Thomson, N.R.: "Fluid Flow in Synthetic Rough Walled Fractures: Navier-Stokes, Stokes, and Local Cubic Law Simulations," *Water Resources Research*, Vol. 39, Issue 4, April 2003.
4. Brown, S.R. and Scholz, C.H.: "Closure of Random Elastic Surfaces in Contact," *Journal of Geophysical Research Solid Earth*, Vol. 90, Issue B7, June 1985, pp. 5531-5545.
5. Snow, D.T.: "Rock Fracture Spacings, Openings, and Porosities," *Journal of Soil Mechanics and Foundations Division*, Vol. 94, Issue 1, 1968, pp. 73-91.
6. Louis, C.: "A Study of Groundwater Flow in Jointed Rock and its Influence on the Stability of Rock Masses," *Rock Mechanics Research Report/Imperial College of Science and Technology*, Vol. 10, 1969, 90 p.
7. Jones Jr., F.O.: "A Laboratory Study of the Effects of Confining Pressure on Fracture Flow and Storage Capacity in Carbonate Rocks," *Journal of Petroleum Technology*, Vol. 27, Issue 1, January 1975, pp. 21-27.
8. Nelson, R.A.: "Fracture Permeability in Porous Reservoirs: Experimental and Field Approach," Ph.D. Dissertation, Texas A&M University, 1975.
9. Gangi, A.F.: "Variation of Whole and Fractured Porous Rock Permeability with Confining Pressure," *International Journal of Rock Mechanics and Mining Sciences & Geomechanics Abstracts*, Vol. 15, Issue 5, October 1978, pp. 249-257.
10. Kranzz, R.L., Frankel, A.D., Engelder, T. and Scholz, C.H.: "The Permeability of Whole and Jointed Barre Granite," *International Journal of Rock Mechanics and Mining Sciences & Geomechanics Abstracts*, Vol. 16, Issue 4, August 1979, pp. 225-234.
11. Walsh, J.B.: "Effect of Pore Pressure and Confining Pressure on Fracture Permeability," *International Journal of Rock Mechanics and Mining Sciences & Geomechanics Abstracts*, Vol. 18, Issue 5, October 1981, pp. 429-435.
12. Gale, J.E.: "The Effects of Fracture Type (Induced vs. Natural) on the Stress Fracture Closure Fracture Permeability Relationships," ARMA paper 82-290, presented at the 23rd U.S. Symposium on Rock Mechanics (USRMS), Berkeley, California, August 25-27, 1982.
13. Seidle, J.P., Jeansonne, M.W. and Erickson, D.J.: "Application of Matchstick Geometry to Stress Dependent Permeability in Coals, SPE paper 24361, presented at the SPE Rocky Mountain Regional Meeting, Casper, Wyoming, May 18-21, 1992.
14. Li, S., Tang, D., Pan, Z., Xu, H., et al.: "Characterization of the Stress Sensitivity of Pores for Different Rank Coals by Nuclear Magnetic Resonance," *Fuel*, Vol. 111, September 2013, pp. 746-754.
15. Chen, D., Pan, Z. and Ye, Z.: "Dependence of Gas Shale Fracture Permeability on Effective Stress and Reservoir Pressure: Model Match and Insights," *Fuel*, Vol. 139, January 2015, pp. 383-392.
16. Zhou, J., Zhang, L., Li, X. and Pan, Z.: "Experimental and Modeling Study of the Stress Dependent Permeability of a Single Fracture in Shale under High Effective Stress," *Fuel*, Vol. 257, December 2019.
17. Jang, H-S., Kang, S-S. and Jang, B-A.: "Determination of Joint Roughness Coefficients Using Roughness Parameters," *Rock Mechanics and Rock Eng*ineering, Vol. 47, Issue 6, January 2014, pp. 2061-2073.
18. Brown, S.R.: "Fluid Flow through Rock Joints: The Effect of Surface Roughness," *Journal of Geophysical Research Solid Earth*, Vol. 92, Issue B2, February 1987, pp. 1337-1347.
19. Zimmerman, R.W., Chen, D-W. and Cook, N.G.W.: "The Effect of Contact Area on the Permeability of Fractures," *Journal of Hydrology*, Vol. 139, Issue 1-4, November 1992, pp. 79-96.
20. Huo, D. and Benson, S.M.: "An Experimental Investigation of Stress and Dependent Permeability and Permeability Hysteresis Behavior in Rock Fractures," Chapter 7 in *Fluid Dynamics in Complex Fractured — Porous Systems*, Faybishenko, B., Benson, S.M. and Gale, J.E. (eds.), 2015, pp. 99-114.
21. Walsh, J.B. and Grosenbaugh, M.A.: "A New Model for Analyzing the Effect of Fractures on Compressibility," *Journal of Geophysical Research Solid Earth*, Vol. 84, Issue B7, July 1979, pp. 3532-3536.
22. Greenwood, J.A. and Williamson, J.P.: "Contact of Nominally Flat Surfaces," *Proceedings of the Royal Society A*, Vol. 295, Issue 1442, December 1966, pp. 300-319.
23. Whitehouse, D.J. and Archard, J.F.: "The Properties of Random Surfaces of Significance in their Contact," *Proceedings of the Royal Society A*, Vol. 316, Issue 1524, March 1970, pp. 97-121.
24. Robin, P-Y.F.: "Note on Effective Pressure," *Journal of Geophysical Research*, Vol. 78, Issue 14, May 1973, pp. 2434-2437.
25. Luo, J., Zhu, Y., Guo, Q., Tan, L., et al.: "Experimental Investigation of the Hydraulic and Heat Transfer Properties of Artificially Fractured Granite," *Scientific Reports*, Vol. 7, 2017.
26. Zimmerman, R.W. and Yeo, I-W.: "Fluid Flow in Rock Fractures: From the Navier-Stokes Equations to the Cubic Law," *Dynamics of Fluids in Fractured Rocks*, Vol. 122, January 2000, pp. 213-224.

About the Authors

Xupeng He

M.S. in Petroleum Engineering, King Abdullah University of Science and Technology

Xupeng He is currently a Ph.D. student at the Ali I. Al-Naimi Petroleum Engineering Research Center, King Abdullah University of Science and Technology (KAUST), Thuwal, Saudi Arabia. His research interests include modeling naturally fractured reservoirs, machine (deep) learning applications in petroleum engineering, and uncertainty quantification and optimization in subsurface flow problems.

Xupeng is the author of 11 conference papers, and two U.S. patents.

He was the recipient of the Excellent Student Cadre and the Outstanding Undergraduate Student Awards in 2014 and 2015, respectively, at Chang'an University. Also, Xupeng received a national scholarship from the Ministry of Education of the People's Republic of China in 2012 and 2013.

He received his B.S. degree in Resource Exploration Engineering (Oil and Gas) from Chang'an University, Xi'an, China, in 2015. Xupeng received his M.S. degree in Petroleum Engineering from KAUST in 2018.

Marwah M. AlSinan

M.S. in Petroleum Engineering, Imperial College

Marwah M. AlSinan joined Saudi Aramco in 2013 as a Petroleum Engineer, working with the Reservoir Engineering Technology Division in the Exploration and Petroleum Engineering Center – Advanced Research Center (EXPEC ARC).

Her research interests include multiphase flow in fractures, carbon dioxide sequestration, and applications of nuclear magnetic resonance in porous media.

In 2013, Marwa received her B.S. degree in Petroleum and Natural Gas Engineering from Pennsylvania State University, State College, PA. She received her M.S. degree in Petroleum Engineering from Imperial College, London, U.K. in 2017.

Dr. Hyung T. Kwak

Ph.D. in Physical Chemistry, Ohio State University

Dr. Hyung T. Kwak joined Saudi Aramco in April 2010 as a Petroleum Engineer with Saudi Aramco's Exploration and Petroleum Engineering Center – Advance Research Center (EXPEC ARC). He had been a member of the Pore Scale Physics focus area (2010 to 2012) and SmartWater Flooding focus area (2013 to 2014) of the Reservoir Engineering Technology Division. Currently, Hyung is a focus area champion of the Pore Scale Physics focus area. His main research focus is seeking deeper understanding of fluid-rock interaction in pore scale of the Kingdom's reservoirs.

Since joining Saudi Aramco in 2010, Hyung has been involved with various improved oil recovery and enhanced oil recovery (EOR) research projects, such as SmartWater Flooding, carbon dioxide EOR, and chemical EOR. Prior to joining Saudi Aramco, Hyung was a Research Scientist at Baker Hughes, with a main area of research related to nuclear magnetic resonance (NMR)/magnetic resonance imaging technology.

In 1996, Hyung received a B.S. degree in Chemistry from the University of Pittsburgh, Pittsburgh, PA, and in 2001, he received his Ph.D. degree in Physical Chemistry from Ohio State University, Columbus, Ohio.

Before moving into the oil and gas industry, Hyung was involved — as a postdoctoral fellow for 2 years — in a project developing the world's largest wide bore superconducting magnet NMR spectrometer, 900 MHz, at the National High Magnetic Field Laboratory.

He has more than 100 publications, including peer-reviewed articles and patents.

Dr. Hussein Hoteit

Ph.D. in Applied Mathematics, University of Rennes 1

Dr. Hussein Hoteit is an Associate Professor in Reservoir Engineering and the Program Chair of Energy Resources and Petroleum Engineering (ERPE) at King Abdullah University of Science and Technology (KAUST), Thuwal, Saudi Arabia.

Before joining KAUST, Hussein worked for ConocoPhillips and Chevron Companies for about 12 years, where he conducted projects related to chemical enhanced oil recovery (EOR), CO_2 EOR, steam flood, EM heating, to name a few.

Hussein's current research includes chemical EOR, geological CO_2 storage, improved oil recovery optimization, data-driven machine learning, and reservoir simulation development.

He has earned several Society of Petroleum Engineers (SPE) awards, including SPE Distinguished Lecturer in 2009, and served as Associate Editor for the *SPE Journal* for more than 10 years.

Hussein received his B.S. degree in Pure Mathematics and Computer Sciences from Lebanese University, Lebanon, M.S. and Ph.D. degrees in Applied Mathematics from the University of Rennes 1, Rennes, France.

Advanced Resistivity Modeling to Enhance Vertical and Horizontal Well Formation Evaluation

Mohamed S. Mahiout, Dr. Chengbing Liu, Ralf Polinski and Moshood Kassim

Abstract /

Accurate formation evaluation relies on, among other inputs, the correct true formation resistivity (Rt). The common practice in the industry is to use the deep resistivity log as Rt. A single resistivity curve from a deep resistivity measurement often does not represent Rt, due to the shoulder bed effect, polarization at the boundaries, and many other effects. This is especially true in high angle and horizontal wells.

The main objective of the article is to demonstrate that advanced resistivity modeling workflows for both wireline and logging-while-drilling (LWD) help in determining the Rt by removing or minimizing the impact of all different effects and improving the formation evaluation in vertical and horizontal wells.

Extensive work and computational advances have provided the oil and gas industry with codes to model resistivity tools in a wide variety of formations/conditions. The workflow used is a model-compare-update approach and provides an interface where a layered Earth model (layer geometry and property) can be constructed. If available, image logs are used to provide dip information for each layer. After several iterations, and if an agreement between the forward model and measured logs has been achieved (called the "reconstruction check"), this will be a confirmation of the structural model and assigned layer properties. Reconstruction of the actual data to the modeled data is the confidence indicator. The model changes or iterations can be done manually or automatically. The practical process is usually a combination of both.

As a result, the resistivity logs free of shoulder bed, polarization, and other effects are extracted as squared logs for each layer and are used to improve the interpretation methodology and minimize the associated uncertainties to reservoir evaluation. The workflow and benefits of advanced resistivity modeling for improving formation evaluation in vertical, and especially high angle and horizontal wells, will be discussed. Several field log examples will be used to demonstrate the capabilities of the proposed workflow to enhance formation evaluation in vertical and horizontal wells. Conclusions from the work with suggestions/recommendations for the way forward will be presented.

Advanced resistivity modeling when used by petrophysicists can have many advantages, especially in complex situations. We propose workflows and case studies that demonstrate the value of such advanced modeling in enhancing the vertical and horizontal well formation evaluation.

Introduction

Resistivity measurements are used extensively in the oil industry for the determination of water saturation. Their accuracy is influenced by several factors such as the right choice of logging tool according to the environmental conditions, the correction for borehole effects, wellbore geometry, formation dip, and other environmental effects. Field logs are usually only corrected for borehole environmental effects such as borehole diameter and borehole fluid resistivity. A simple 1D correction for borehole fluid invasion effects may be performed to obtain an invasion corrected formation resistivity (Rt) and invaded zone (or shallow) resistivity (Rxo).

Other environmental effects can have a great impact on the accuracy of resistivity logs. Yet, field logs are typically not corrected for additional effects before they are used in a saturation analysis. Environment variables like porosity and shale volume are dealt with in the petrophysical evaluation using appropriate saturation equations.

The other most common effects discussed in the literature are the presence of thin beds (where standard resistivity logs might suffer from poor vertical resolution or low resistivity pay), dipping formations or deviated wellbores (where the relative angle between the wellbore and the formation creates issues with the tool's large depth of investigation or creates polarization horns), high resistivity contrast between tight and porous layers (shoulder bed effects), and anisotropic formations[1-5]. These environmental effects require advanced corrections as they are no longer 1D, but multidimensional (2D or 3D). The impact of those environmental corrections on true formation resistivity, i.e., water saturation, are significant, especially for complex formations such as thin beds and horizontal injectors drilled in high water intervals[6, 7].

The main interpretation objective (and challenge) is to invert the measured data to solve for the true resistivity values across the different zones of the reservoir probed by the tool. Inversion can carry a lot of uncertainties as the logging tools can be sensitive to the resistivity of multiple layers at the same time. Uncertainties could also result from borehole enlargement, high standoff, and the assumption of zero invasion on data acquired while drilling.

Wireline and LWD Resistivity Basics and Job Planning Considerations

Formation resistivity can be measured using logging-while-drilling (LWD) electromagnetic (EM) propagation or laterolog tools, or after drilling using cable deployed (wireline) induction or laterolog tools. Today, all modern resistivity tools are the array type with multiple spacings and multiple depth of investigation, which derive Rt typically through an inversion processing.

Modern wireline induction tools generate multiple induction responses at an integrated radial response of typically 10", 20", 30", 60", and 90" from the center of the borehole. Likewise, the array laterolog tools generate multiple galvanic responses of varying depth of investigation[8].

Induction measurements can operate in water-based and nonconductive borehole environments, which makes them the only resistivity measurement available in oil-based mud. Induction tools respond to the conductivity of the formation. They can be considered as measuring the formation resistivity in parallel, Fig. 1. As a conductivity sensitive measurement, an induction tool is preferred for a low formation resistivity environment, and in the case of resistive invasion of borehole fluid into the formation (Rxo > Rt)[9].

LWD laterolog and propagation tools are similar to wireline tools and use different frequencies and spacings. These differences manifest in higher vertical resolution, shallower depth of investigation, higher polarization, and anisotropy effects. LWD EM propagation tools measure two types of resistivity, phase shift, and attenuation. These resistivities have different depths of investigation where the deepest phase has a shallower depth of investigation than the shallower attenuation. In laminated reservoirs the attenuation is more affected by the shoulder beds' effect, due to its deeper depth of investigation.

Laterolog measurements require a conductive borehole fluid to allow the measurement current to traverse the borehole into the formation. Laterolog measurements respond to the resistivity of the formation in series, and are preferred over induction tools when the contrast between the formation resistivity and borehole resistivity is high, and in cases of conductive invasion (Rxo < Rt).

The choice of a resistivity tool is based on the borehole fluid type, well deviation and the environmental conditions, which can be confirmed with tool planner modeling.

The basic wellsite processing of all modern array resistivity tools comes with a simple 1D radial processing to correct for borehole fluid invasion into the reservoir zones and provide an invasion corrected Rt and invaded zone Rxo. Other effects are usually not corrected for in the basic processing and must be addressed during post-acquisition processing.

Reservoir Challenges and Resistivity Modeling

In the beginning of resistivity logging all that existed was the logged data. With time came log correction charts, then simple 1D correction software to correct for invasion, or bed thickness/vertical resolution, or account for other single environmental effects like anisotropy. Later, other software tried to solve for 2D effects and dip. They were slow, cumbersome, and limited in scope.

Today, extensive work and computational advances provide the oil and gas industry with codes to model resistivity tools in a wide variety of formations/conditions. Figure 2 shows a model-compare-update approach

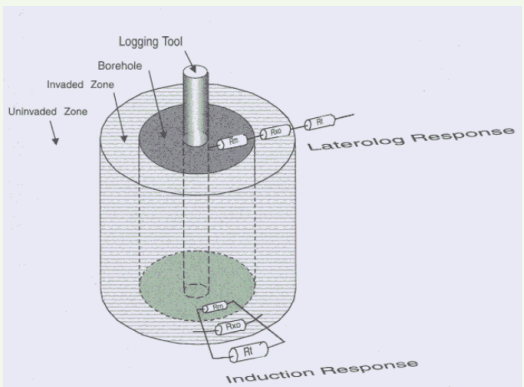

Fig. 1 *Laterolog tools are sensitive to the series of resistivity types that the measurement current traverses. Induction tools are sensitive to formation conductivity, which can be can also be expressed as being sensitive to resistivities in parallel[8].*

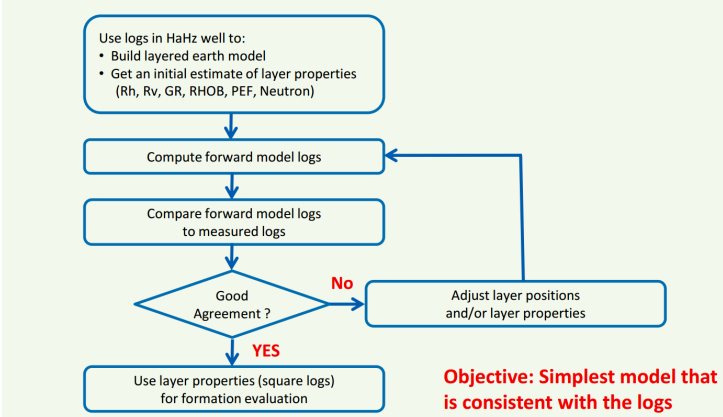

Fig. 2 *An example of a model-compare-update approach workflow for advanced resistivity modeling, in this case for high angle/horizontal wells[10].*

workflow used, and provides an interface where a layered Earth model (layer geometry and property) can be constructed.

The layered Earth model assumes that the layers are laterally extensive, and the properties of each layer do not change. When the same layer is crossed multiple times in a high angle or horizontal well, variations of properties can be observed along the well path. When this occurs, lateral property boundaries are inserted into the model. If available, image logs provide dip information for each layer. In high angle wells, image logs are essential to build and constrain the structural model. After several iterations, and if an agreement between the forward model and measured logs has been achieved (called the "reconstruction check"), this will be a confirmation of the structural model and assigned layer properties.

Reconstruction of actual data to modeled data is the confidence indicator. The model changes or iterations can be done manually or automatically. The practical process is usually a combination of both.

In vertical or low angle wells, the typical challenges with resistivity logs are shoulder bed effect, adjacent bed effect (dipping beds/relative dip), and resistivity anisotropy (not discussed in the context of this article).

The shoulder bed effect describes the effect of high resistivity contrast between adjacent beds. Figure 3 illustrates a simple case of a low resistivity bed with Rt of 1 ohm.m located between high resistive shoulder beds of 1,000 ohm.m (also called squeeze effect). The deep resistivity curve in the low resistivity bed is affected by the high resistivity shoulder and reads too high. Shallower curves are also affected resulting in an erroneous invasion profile.

The dipping layer or relative dip effects describe the impact of dipping beds in case of a vertical borehole, or a horizontal bed penetrated by a deviated borehole. The traditional interpretation of resistivity measurements assumes the formation bedding is perpendicular to the tool axis. In the presence of high relative dip, this is no longer true, as the tool's response is usually deep enough that it includes or encompasses multiple layers at the same time, and the situation becomes a 2D or 3D problem.

This effect also depends on the interplay between the bed's thickness and the measurement depth of investigation (DOI). If the dipping beds are thick compared to the measurement DOI, the effect will only be felt when the borehole crosses the bed boundaries, where polarization horns could be generated depending on the resistivity contrast and the relative dip. If the dipping beds are thin compared to the measurement DOI, the resistivity measurement will always be sensitive to the resistivity of the adjacent beds.

Figure 4[11] illustrates the case of an induction log response at 0° relative dip (right) and 70° relative dip (left). While the logs are focused into the bedding at 0°, their response is affected by the beds above and below at the higher relative dip, which leads to a reading of the deeper

Fig. 3 *Laterolog squeeze effect in case of a 1 ohm.m layer between 1,000 ohm.m shoulder beds. The deep measurements in the low resistivity bed read too high and show an erroneous invasion profile, even though the formation may be uninvaded.*

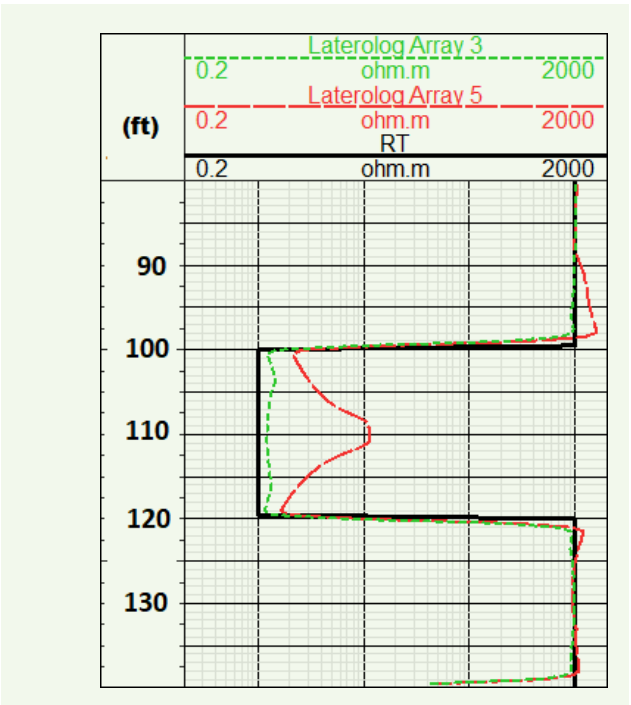

Fig. 4 *The effect of dip on induction logs. Logs which are focused into the bedding when the well inclination is at 0°, are sensitive to the resistivity from beds above and below at the higher relative dip, and deep reading curves either read too high or too low[11].*

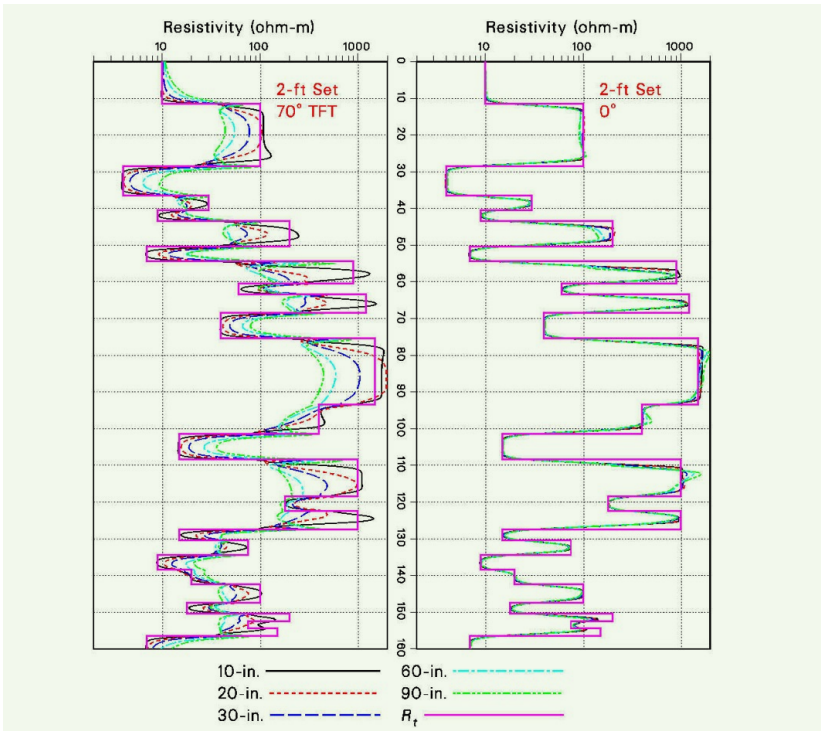

curves that is either too high or too low.

In high angle wells the three main effects that can be encountered, single or in combination, are anisotropy, invasion, and shoulder beds (thin beds, boundary, and proximity). Figure 5[12] is a simple model of a formation logged at an 89° hole angle. The reservoir is 10 ft true vertical depth (TVD) thick, is drilled within a 500 ohm.m layer and sandwiched between shale layers of 2 ohm.m resistivity. The graph illustrates what we should see with a 2 MHz LWD propagation resistivity tool with no invasion in a clean homogenous formation. We see polarization horns at the layer transition. In the center, we see the proximity bed effect.

The net effects are that high resistivity in the shale near the sand would produce a false hydrocarbon reading, and the high resistivity at the top and bottom of the sand would cause the overestimation of the hydrocarbon saturation. The center of the sand shows a resistivity below Rt, which would cause an overestimation of the water saturation. Another interesting effect is that in the center of the reservoir the deeper reading curves are reading lower than the shallow resistivity curves as more of their volume of investigation is in the shale compared to the shallower curves.

The net effect is that the deepest curves are pulled down more than the shallower ones, and the effect looks like a resistive invasion profile. The thinner the bed the more pronounced the difference between the true Rt and the apparent measured resistivity will be. If the situation was reversed and the reservoir was 2 ohm.m and the layers above and below were 500 ohm.m, the measured resistivity in the middle of the layer would be higher than the Rt. Understanding the reservoir structure and the position of the logged wellbore within it is important to improving the evaluation.

The following examples demonstrate that the deep resistivity measurement does not always represent Rt, due to shoulder beds, polarization, and many other effects.

Field Example/Applications

The first field example shows wireline laterolog resistivity data from a vertical well penetrating a series of tight, high resistive anhydrite layers and thinner, porous and low resistivity carbonate intervals. The laterolog array resistivity tool was run in this well due to the large borehole diameter and high salinity water-based mud, which creates a large contrast of the measured formation resistivity to mud resistivity (Rt/Rm).

Figure 6[13] displays a tool planner chart for the operating range of induction measurements. The chart shows that only the 4 ft resolution induction log are suitable in this environment, but only up to a formation resistivity of approximately 20 ohm.m.

The laterolog field data, including a 1D radial invasion corrected Rt, show curve separation from shallow to deep curves in the target layers, indicating an apparent conductive invasion profile. The petrophysical analysis shows an apparent low water saturation in the thin carbonate layers, contrasting with local knowledge and the results of a dielectric dispersion log also acquired

Fig. 5 *A modeled 2 MHz phase shift polarization horn and shoulder bed effect at 89° hole angle, 10 ft TVD thick bed. It shows the bed boundary effects and an apparent resistive invasion profile in the center of the bed. The light blue is deep, dark blue is medium; black is shallow resistivity[12].*

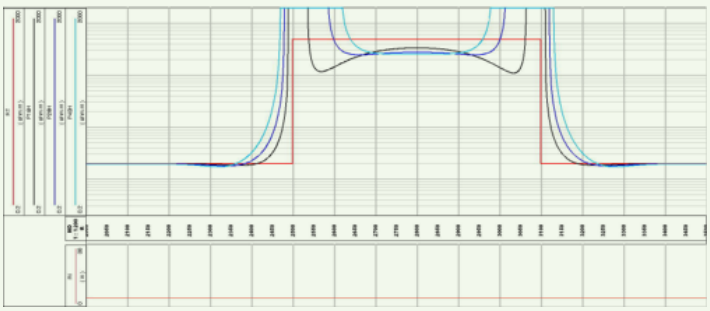

Fig. 6 *The resistivity tool planner charts with operating envelope of the induction tool for the environment of example 1. The left chart shows only 4 ft resolution curves are suitable in this environment for lower resistivity. The right chart shows that 4 ft curves leave suitable range at ~20 ohm.m expected formation resistivity. The laterolog will be preferred if formation resistivity is larger, but induction will be preferred in low formation resistivity (tool planner based on Barber 1999)[13].*

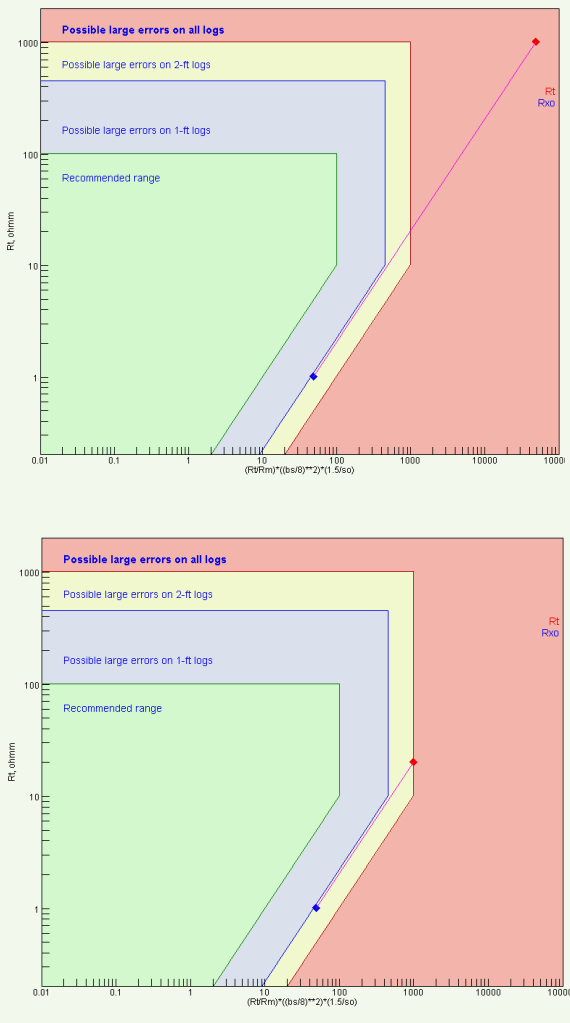

in this well, Fig. 7.

The laterolog response in this environment of low resistivity carbonate beds within high resistivity anhydrite layers, however, can also be explained as a classic case of shoulder bed or "squeeze" effect. To test this hypothesis, a synthetic formation model was built using induction resistivity information from a nearby well, which indicated that the true resistivity of the low resistivity carbonate layers should be approximately 1 ohm.m.

A first model was built considering only the shoulder bed effect on the laterolog data, Fig. 8, by using a 1D model type. The resistivity from the nearby well (1 ohm.m) was used as an initial estimate of the true formation resistivity. The resistivity logs were forward modeled and compared to the measured logs. The forward modeled array 5 curve shows a good match to the measured array 5 curve confirming that the observed high reading is most likely caused by the shoulder bed effect of the neighboring tight anhydrite layers. The modeled array 3 response, however, suggests an additional effect is responsible for the observed difference of modeled vs. measured curve, as the measured curve reads higher than the modeled array 3.

A second model introduces resistive mud filtrate invasion with a filtrate salinity lower than formation water salinity, now making a 2D model of layering and invasion. The Rxo model was derived from the measured microresistivity log. Figure 9 shows that the modeling results (in track 5) now compare well with the measured array 3 and array 5 curves. It confirms that the measured laterolog curve readings can be explained as a combination of the shoulder bed effect and resistive invasion of lower salinity mud filtrate into higher salinity formation water. The new interpretation using the modeled Rt as input to the petrophysical analysis is now consistent with field observations in nearby wells and the results of the dielectric log, Fig. 10.

The second field example is from wireline induction logs across a deviated/high angle well, which penetrated a sequence of clean sandstone and shaly layers. Bed boundary effects were observed across the logs, and a large polarization horn was present across the oil-water contact (OWC), Fig. 11.

The OWC picked by the deep induction resistivity logs distinctively appears about 12 ft deeper than the neutron-density logs. Figure 12 shows the high angle

Fig. 7 *Triple combo logs across a series of tight anhydrite layers and thinner porous carbonates. The saturation analysis using Rt from a 1D (radial invasion) inversion shows an apparent hydrocarbon saturation of ~50% not matching local field knowledge and advanced logs from the same well. The red box shows the intervals of Figs. 8, 9, and 10.*

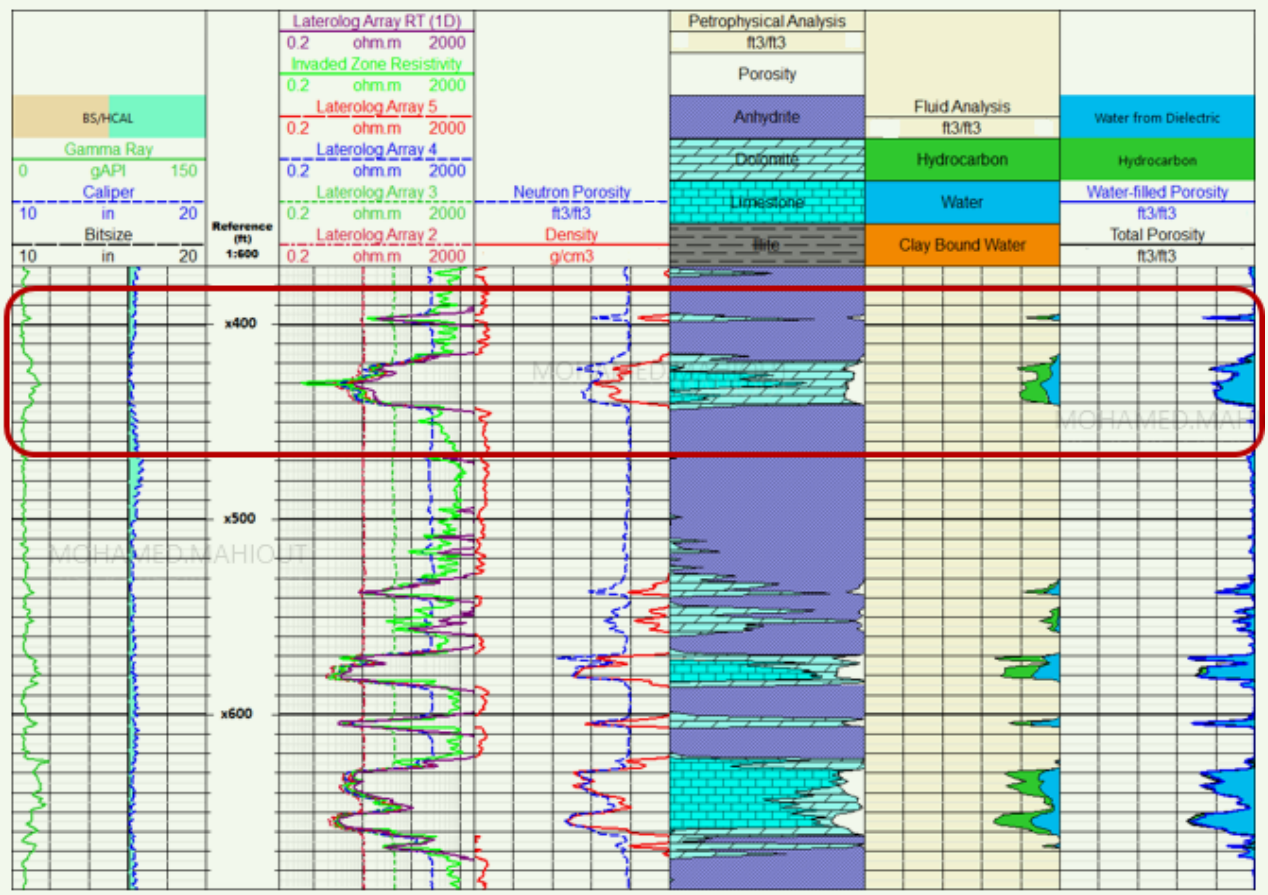

Fig. 8 *A detailed view of two carbonate layers within the tight anhydrite interval. The separation of the single array resistivity curves shows an apparent invasion of conductive borehole fluid into a higher resistive bed. A formation model Rt curve built from nearby well information in track 4 is displayed together with the measured laterolog Rt. The dashed curves in track 5 show the modeling of array 3 and array 5 modeled considering only shoulder bed effect without any invasion. The array 5 measured curve compares well to the modeled array 5 curve, suggesting that the high reading is almost entirely caused by the shoulder bed effect. The modeling doesn't reconstruct array 3 very well, indicating that another factor is contributing to the measurement.*

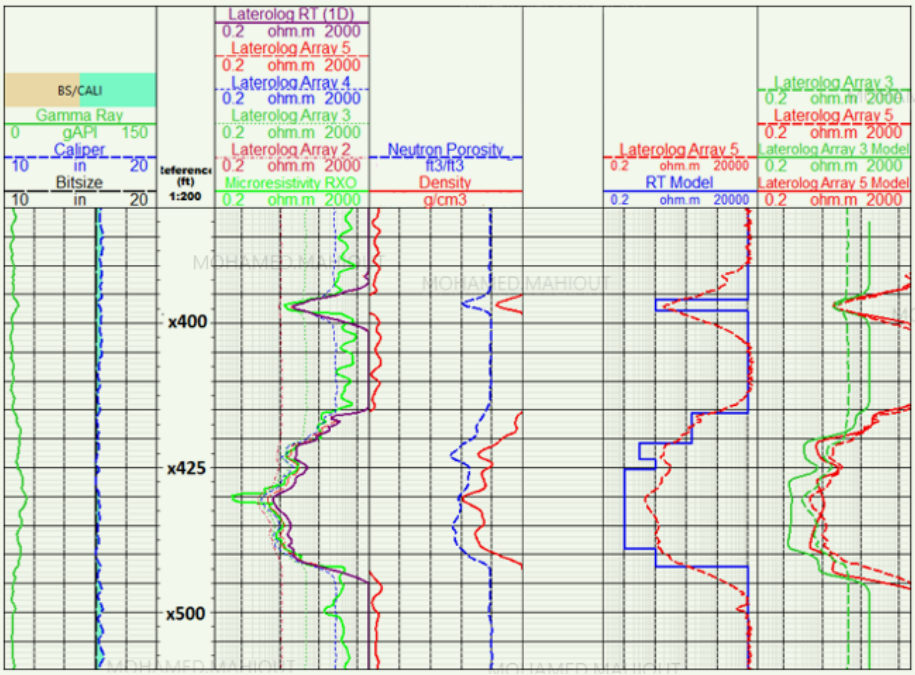

Fig. 9 *The formation model, including invasion effect in addition to the shoulder bed effect. Track 5 shows the modeled array 3 and array 5 curves (dashed) now matching the measured array 3 and array 5 curves. Therefore, the resistivity response in this layer can be explained as a combination of the shoulder bed effect and resistive invasion.*

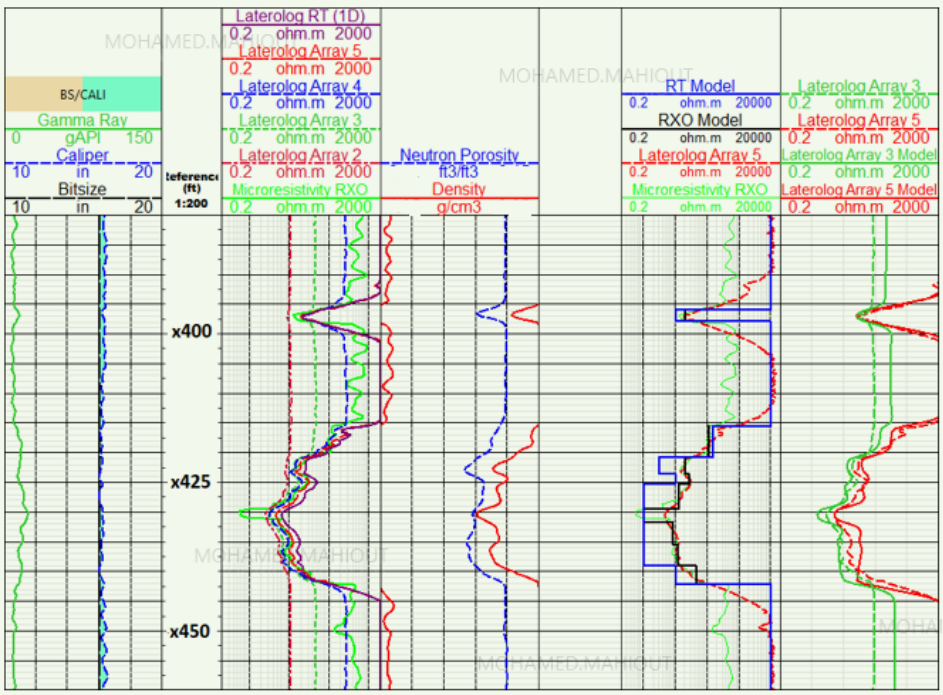

Fig. 10 *A comparison of fluid analysis. The left track shows the initial analysis using the measured laterolog Rt. The middle track shows the analysis using the modeled Rt, and the right track shows the fluid analysis from the dielectric log. The analysis using the modeled Rt is consistent with the dielectric analysis.*

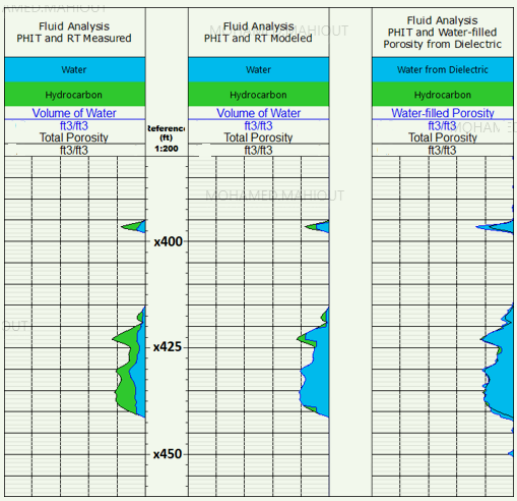

Fig. 11 *Triple combo logs across a sequence of clean sandstone and shaly layers. The red box shows the huge polarization horn on the induction logs at the OWC, and the depth discrepancy between the OWC from the deep induction logs and the neutron-density logs.*

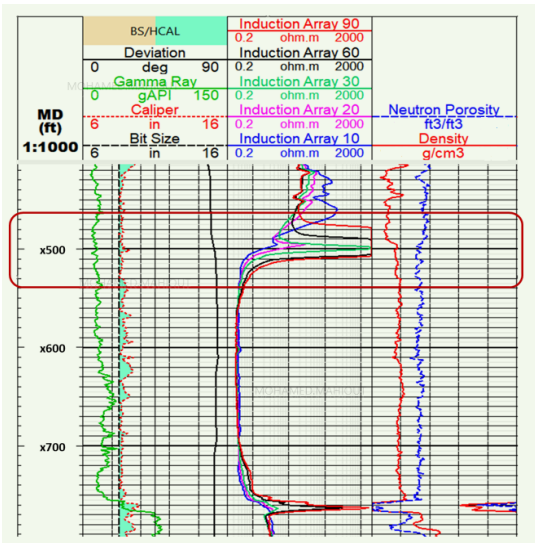

resistivity modeling was done across this OWC. The model code used was 1D + dip, which assumes the measurements are affected only by layering and formation dip. The dominant effects at the zone of interest appear more geometrically related, therefore, the assumption of zero to very minimal invasion seems valid. LWD density images provided the dip data.

Fig. 12 *Curtain section of a high angle well modeling using wireline induction logs. The first track of the upper panel shows the 60″ and 90″ 4 ft measured resistivity logs (induction array 60 and 90), and the forward modeled logs (induction array 60_FM, and 90_FM). The second track of the upper panel shows a comparison of the 60″ and 90″ measured resistivity logs and the corrected true resistivity squared log (RH_SQR) at the OWC. The bottom panel shows the 2D geometry of the curtain section, with different layers indicated by the thin black markers and blue circles. The layer colors indicate the horizontal resistivity. The horizontal axis is the true horizontal length.*

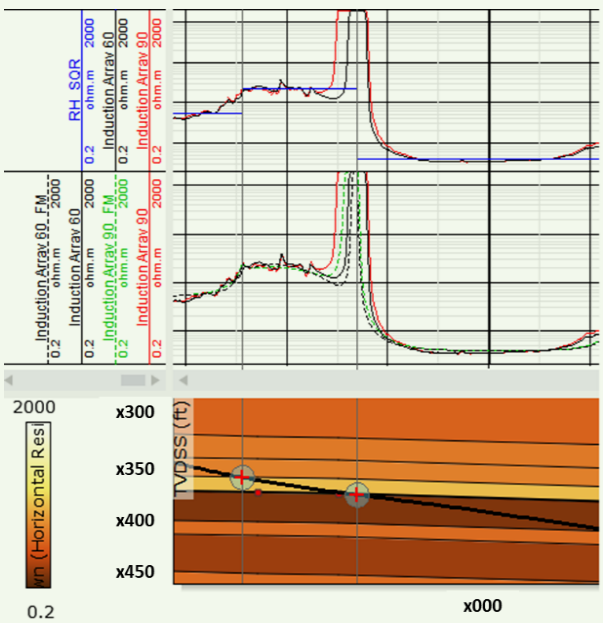

The model was constructed using the wireline triple combo logs, and formation dips. The initial true formation resistivity was defined from the measured induction array 90. The resistivity logs were forward modeled, and subsequent adjustments were made on the geometry and formation resistivity using an iterative model-compare-update approach. The final modeled logs did show a good match with the measured logs. They reproduced the polarization horn across the OWC, Fig. 12, which shows a comparison between the induction arrays 60 and 90 and their respective forward modeled logs. The match indicates that the model is a valid representation of the geometry and layer properties of the formation. The corrected Rt now agrees with the density-neutron logs regarding the depth of the OWC. Additionally, the water saturation analysis using the corrected Rt did show a much higher water saturation at the OWC than the initial analysis using the measured logs, Fig. 13.

The third example shows LWD logs from an 8½” borehole that was drilled through a sequence of carbonate layers interbedded with siltstone and/or shale, Fig. 14. The hole deviation was 70° to 82°, indicating that the propagation resistivities would likely be affected by the nearby layers, which is confirmed by the numerous polarization horns.

Figure 15 displays the curtain section of the formation model for the entire well using the advanced resistivity

Fig. 13 *A comparison of water saturation analysis. The third and fourth tracks show that the modeled Rt (RH_SQR) agree well with the OWC picked by the neutron-density logs. The fifth track shows the initial water saturation analysis using the measured induction array Rt. The last track shows the recomputed water saturation analysis using the modeled Rt. The difference in water saturation analysis is very visible within the red box.*

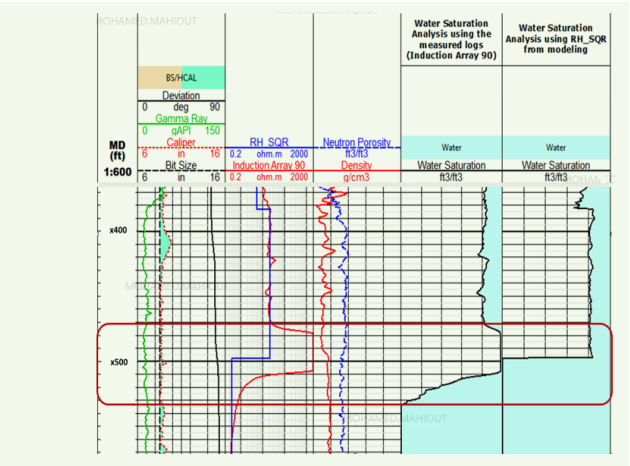

Fig. 14 *The LWD triple combo logs across a series of carbonate and shale sequences.*

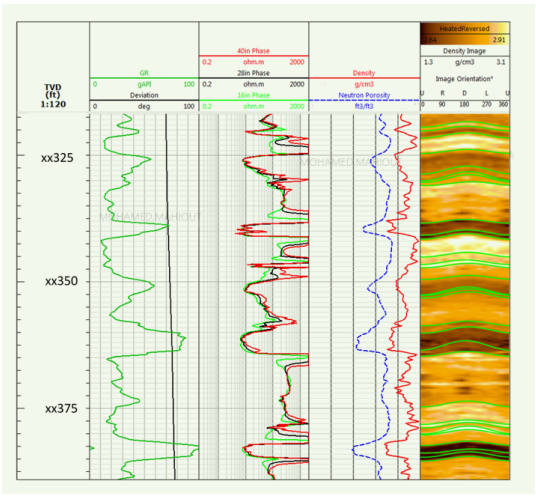

modeling workflow. The goal was to build the simplest model that is consistent with the measured logs. The modeling type used was 1D + dip. Zero invasion is assumed since invasion is usually not a dominant factor on LWD logs and this allows the modeling to focus on the geometrical effects on the logs. Formation dips were extracted from the density image logs, and the layered Earth model was constructed using all the logs and dip sinusoids. Each layer within the structural model was then populated with initial estimates of resistivities using the median of the measured 40" phase and 40" attenuation as vertical (RV) and horizontal resistivities (RH), respectively.

Fig. 15 *The curtain section of a LWD high angle well that shows the subsurface model across the trajectory. The upper panel shows the 16" and 40" measured resistivity logs (16" and 40" phase, 16" and 40" attenuation), the forward modeled logs (16" and 40" Phase_FM, 16" and 40" Attenuation_FM) and the corrected true resistivity squared logs (RH_SQR). The bottom panel shows the 2D geometry of the curtain section with different layers indicated by the thin black markers and blue circles. The layer colors indicate the horizontal resistivity. The horizontal axis is true horizontal length. The blue squared curve is the modeled Rt. The black dashed curves are modeled 16" phase and attenuation. The dashed green curves are modeled 40" phase and attenuation. Solid black curves are measured 16" phase and attenuation. Solid red curves are measured 40" phase and attenuation.*

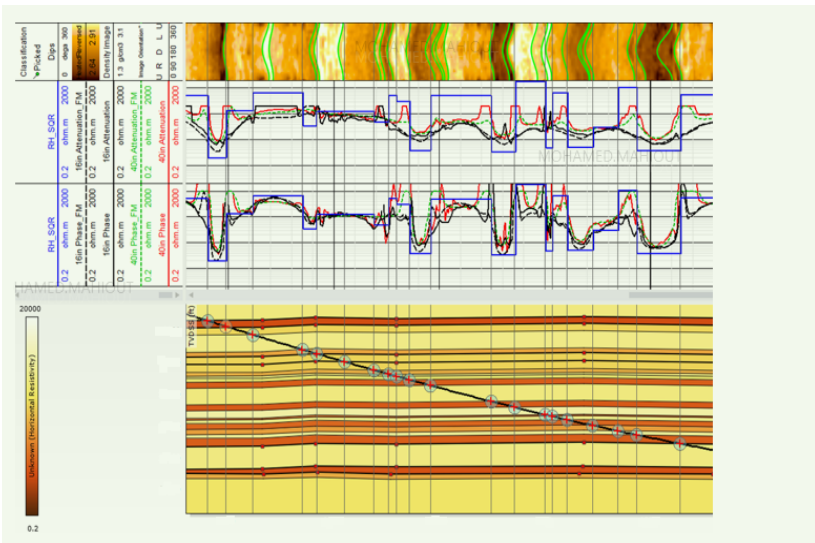

The forward model logs were computed and the structural model and layer resistivities were adjusted until a good match between the modeled curves and the measured logs was obtained across most intervals. Figure 15 also shows a comparison between the measured 16" phase, 16" attenuation, 40" phase, 40" attenuation and their respective forward modeled logs. It is easy to see the difference between the modeled Rt (RH_SQR) and measured curves across many intervals due to the nearby beds effect. Instinctively, we make the assumption that the deepest reading curve is always closer to the Rt. In fact, the deeper the resistivity reads, the more it is affected by the shoulder beds and the shallower resistivity curve might actually be closer to the Rt in high angle wells, Fig. 16.

Conclusions

Resistivity logs can be affected by several effects, which are not accounted for in the standard field processing. Advanced resistivity modeling workflows to simulate these effects can have many advantages in getting a more accurate true formation resistivity, especially in complex situations or for evaluating horizontal water injectors. This requires additional inputs, and could be time-consuming. Additionally, we need to consider the uncertainties related to the model assumptions.

Fig. 16 *A comparison of all phase and attenuation curves with Rt. Rt is seen to be closer to the phase curves than the attenuation curves since the attenuation curves read deeper into the formation, and therefore, are more affected by nearby beds.*

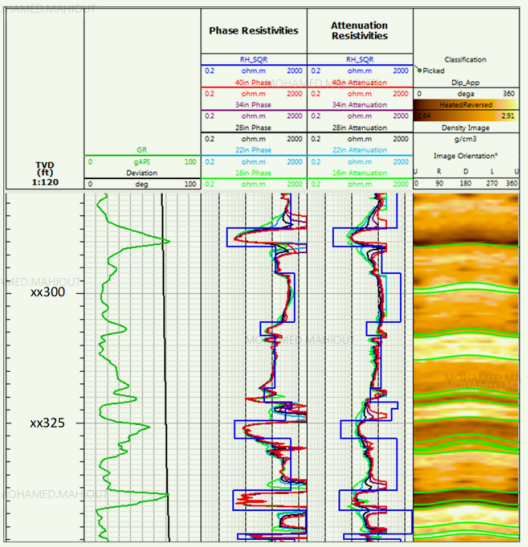

Fig. 17 *Advanced resistivity processing workflow for both low and high angle wells.*

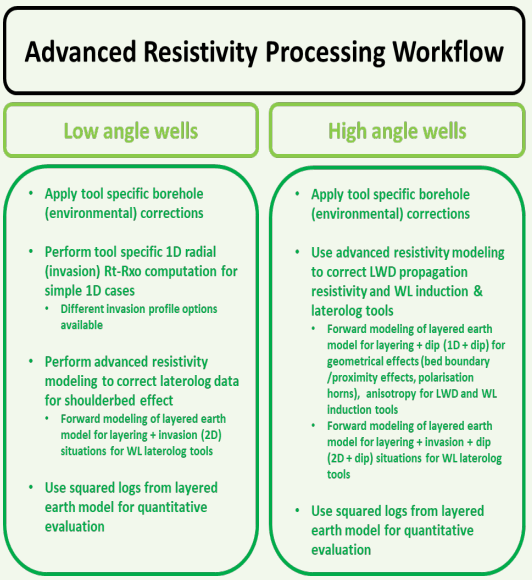

We have demonstrated in three case studies for both wireline and LWD measurements how advanced resistivity modeling can enhance the formation evaluation in vertical and horizontal wells. These and similar workflows are encouraged to be used especially in ambiguous situations.

A proposed customized resistivity processing workflow, Fig. 17, has been put together for both low angle (vertical and near vertical) and high angle (horizontal and highly deviated) wells.

Acknowledgments

This article was prepared for presentation at the Abu Dhabi International Petroleum Exhibition and Conference, Abu Dhabi, UAE, November 9-12, 2020.

References

1. Barber, T. and Rosthal, R.A.: "Using a Multiarray Induction Tool to Achieve High-Resolution Logs with Minimum Environmental Effects," SPE paper presented at the SPE Annual Technical Conference and Exhibition, Dallas, Texas, October 6-9, 1991.
2. Anderson, B.I., Barber, T.D. and Lüling, M.G.: "The Response of Induction Tools to Dipping, Anisotropic Formations," paper presented at the SPWLA 36th Annual Logging Symposium, Paris, France, June 26-29, 1995.
3. Klein, J.D., Martin, P.R. and Allen, D.F.: "The Petrophysics of Electrically Anisotropic Reservoirs," paper presented at the SPWLA 36th Annual Logging Symposium, Paris, France, June 26-29, 1995.
4. Legendre, E., Dubourg, I., Doduy, J., Smits, J.W., et al.: "Better Saturation from New Array Laterolog," paper presented at the SPWLA 40th Annual Logging Symposium, Oslo, Norway, May 30-June 3, 1999.
5. Galli, M.T., Gonfalini, M., Mele, M., Belik, P., et al.: "Resistivity Modeling of Array Laterolog Tools: An Application in an Offshore Norway Clastic Reservoir," *SPE Reservoir Evaluation & Engineering*, Vol. 8, Issue 1, February 2005, pp. 77-87.
6. Al-Hajari, A.A., Ma, S.M., Geier, R., Butt, P.J., et al.: "Constrained LWD Resistivity Modeling for Improved Formation Evaluation of Horizontal Water Injectors," SPE paper 103684, presented at the International Oil and Gas Conference and Exhibition in China, Beijing, China, December 5-7, 2006.
7. Ma, S.M., Al-Hajari, A., Butt, P.J. and Crary, S.F.: "Formation Evaluation of Horizontal Water Injectors Drilled in Thick Carbonate Reservoirs: Behind Casing Analysis and LWD Resistivity Modeling," SPE paper 102572, presented at the SPE Annual Technical Conference and Exhibition, San Antonio, Texas, September 24-27, 2006.
8. Griffiths, R., Barber, T. and Faivre, O.: "Optimal Evaluation of Formation Resistivities Using Array Induction and Array Laterolog Tools," paper presented at the SPWLA 41st Annual Logging Symposium, Dallas, Texas, June 4-7, 2000.
9. Crary, S., Jacobsen, S., Rasmus, J.C. and Spaeth, R.: "Effect of Resistive Invasion on Resistivity Logs," SPE paper 71708, presented at the SPE Annual Technical Conference and Exhibition, New Orleans, Louisiana, September 30-October 3, 2001.
10. Griffiths, R., Morriss, C., Ito, K., Rasmus, J., et al.: "Formation Evaluation in High Angle and Horizontal Wells — A New and Practical Workflow," paper presented at the SPWLA 53rd Annual Logging Symposium, Cartagena, Columbia, June 16-20, 2012.
11. Barber, T.D. and Shray, F.: "Case Studies Using Advanced Interpretation Techniques for Induction Logs," SPE paper 71707, presented at the SPE Annual Technical Conference and Exhibition, New Orleans, Louisiana, September 30-October 3, 2001.

12. Bourg, L.M., Decoster, E., Klein, J. and Gipson, L.: "Resistivity Logging in Horizontal Wells in the Orinoco Heavy Oil Belt: Laterolog or Dielectric Propagation LWD Tools?" paper presented at the SPWLA 48th Annual Logging Symposium, June 3-6, 2007.

13. Darling, H., Barber, T., Wu, X. and Sijercic, Z.: "Interpreting Multiarray Induction Logs in Difficult Environments," paper presented at the SPWLA 40th Annual Logging Symposium, Oslo, Norway, May 30-June 3, 1999.

About the Authors

Mohamed S. Mahiout

M.S. in Geostatistics, Paris School of Mines

Mohamed S. Mahiout is a Petroleum Engineer working in Saudi Aramco's Gas Petrophysics Unit of the Reservoir Description and Simulation Department. He has 30 years of experience, which includes wireline, logging-while-drilling, and geosciences.

Mohamed started his career with Sonatrach working as a Petrophysicist and then as the Head of the Petrophysics Department.

He later joined Schlumberger and served as a Logging Engineer in many locations, including Canada, Brazil, Oman, and Iran, and later as the Petrophysics Domain Champion in Angola and India. Following that, Mohamed joined Baker Hughes as a Geoscience Manager in Qatar.

He is the author of several papers.

Mohamed is a member of the Society of Petroleum Engineers (SPE) and the Society of Petrophysicists and Well Log Analysts (SPWLA).

He received his M.S. degree in Geostatistics from the Paris School of Mines, Paris, France.

Dr. Chengbing Liu

Ph.D. in Geology, Geology Institute of Chinese Academy of Science

Dr. Chengbing "CB" Liu was a Petrophysics Consultant working in the Advanced Petrophysical Modeling Group of Saudi Aramco's Reservoir Description and Simulation Department before his recent retirement. His technical focus was low resistivity/low resistivity contrast pay identification, new applications of electrical/di-electrical logging via integrating with nuclear magnetic resonance (NMR)/wireline formation test, and horizontal well log interpretation.

Before joining Saudi Aramco, CB worked for Chevron for 10 years in Kuwait and the U.S. Before Chevron, he worked for Schlumberger for 14 years in China, Malaysia, and the U.S. Prior to this, CB worked for CNPC for a few years in China.

He is an Associate Editor for the *Journal of Petrophysics*. CB has published two books and 25 papers. He holds 12 U.S. granted patents.

CB received his B.S. degree in Petrophysics from the China Petroleum University, Beijing, China, and his Ph.D. degree in Geology from the Geology Institute of Chinese Academy of Science, Beijing, China.

Dr. Ralf Polinski

Ph.D. in Geology, Karlsruhe Institute of Technology

Dr. Ralf Polinski was a Principal Petrophysicist and Wireline Petrophysics Domain Champion for Schlumberger Middle East, based in al-Khobar, Saudi Arabia, until his retirement in July 2020. He joined Schlumberger in 1992 as a Geologist and since has held a variety of positions in management, interpretation, and sales/marketing in the Middle East, West Africa, Latin America, and Europe.

In his past position in Saudi Arabia, Raif supported the acquisition and interpretation of wireline petrophysical and acoustic measurements, introduction of new technology, and joint research activities in Saudi Arabia and Bahrain.

He received his Ph.D. degree in Geology from Fredericana University, Karlsruhe, Germany (now Karlsruhe Institute of Technology).

Moshood Kassim

M.S. in Petroleum Engineering, King Fahd University of Petroleum and Minerals

Moshood Kassim is currently a Senior Petrophysicist working for Schlumberger Middle East with 8 years of industry experience. He provides petrophysical support and interpretation to logging-while-drilling and wireline measurements.

Moshood received his B.S. degree in Chemical Engineering from Obafemi Awolowo University, Ife, Nigeria, and his M.S. degree in Petroleum Engineering from King Fahd University of Petroleum and Minerals (KFUPM), Dhahran, Saudi Arabia.

An Acoustic-Based Method for Measuring Surfactant Concentration in Field Applications

Hala A. AlSadeg, Jesus M. Felix Servin and Dr. Amr I. Abdel-Fattah

Abstract /

Numerous enhanced oil recovery (EOR) techniques entail injecting chemical treatments such as surfactants at a predetermined concentration to achieve targeted results. Typically, these formulations are prepared on-site using large mixing tanks, prior to injection into the reservoir. The current quality assurance practice for proper concentration of treatment materials uses indirect methods such as interfacial tension (IFT) and/or viscosity measurements. These measurements can be lengthy or only suitable for a specific range of dispersed phase volumes.

We examined the prospect of using acoustic measurements — ultrasound — as a method to determine surfactant concentration for quality assessment of chemical injections on-site. The advantage of ultrasound is that it can characterize both concentrated systems and low dispersed phase volumes.

In this study, we acquired the sound attenuation of an amphoteric surfactant, cocamidopropyl hydroxysultaine (CBS), and in-house petroleum sulfonate surfactant nanocapsules (nanosurfactant), within a frequency range of 3 MHz to 99.5 MHz. We conducted a set of experiments to establish the relationship between acoustic attenuation and surfactant concentration, and assess the measurements' dependence on variable factors, including applied frequency, suspending fluid, and temperature.

The data showed a nearly perfect linear fit in the higher frequency range — 65 MHz to 99.5 MHz — where the coefficient of determination was between 0.979 and 0.998. Consistent with theoretical predictions, this method showed sensitivity to water salinity where the surfactant — at a constant concentration — displayed higher attenuation values in response to the increase in water salinity, allowing the contribution of surfactants to the acoustic attenuation to be isolated. Our method accurately determined surfactant concentrations using acoustic attenuation regardless of the surfactant used.

Adopting such a robust protocol that can determine the surfactant concentration and has the potential to improve field quality assurance methods would be beneficial for EOR research and industry applications whether as a stand-alone system or in conjunction with other commonly available methods.

Introduction

Enhanced oil recovery (EOR) is an active field of research that strives to maximize the recovery factor of hydrocarbon reservoirs[1]. Among multiple EOR strategies available, surfactant EOR has been attracting attention lately[2]. Surfactant EOR entails injecting surfactants at predetermined concentrations to reduce interfacial tension (IFT) between oil and water, and displace oil that would not flow under primary or secondary production. For over a decade, surfactants displayed a great potential to enhance the residual oil mobility either by reducing the IFT between oil and water or by altering the rocks' wettability, even in high temperature and high salinity/hardness conditions[3-7]. Studies even showed that many surfactant formulations succeed to reduce IFT to an ultra-low-region of 0.001 dyne/cm using a significantly low concentration of approximately 1 ppm to 10 ppm[8].

One of the main challenges of surfactant manufacturing scaleup, from laboratory to large-scale, is to maintain product consistency. To achieve optimal results at a minimal cost, it is critical to adjust the surfactant solution to obtain the desired phase-behavior at reservoir conditions. If the concentration is too low, the effect may not be enough. If the concentration is too high, the treatment may not be cost-effective. Typically, these formulations are prepared on-site prior to injection into the reservoir using large mixing tanks. The current quality assurance practice for proper concentration of treatment materials uses indirect methods such as IFT and/or viscosity measurements. These measurements can be lengthy, or only suitable for a specific range of dispersed phase volumes. Therefore, there is a need for new approaches that can accurately quantify surfactant concentration quickly and easily.

Nanosurfactant is an in-house developed reservoir nanoagent technology with a great potential for EOR applications[9, 10]. It consists of 10 nm to 60 nm of petroleum sulfonate containing oil droplets dispersed in high salinity water. Petroleum sulfonate, which is abundant and inexpensive, but insoluble high salinity water is stabilized via a special class of co-surfactants. Being able to measure the nanosurfactant concentration on-site quickly and easily is an essential quality assessment component to ensure a successful field implementation.

In this work, we propose a method based on acoustic attenuation measurements to quantify nanosurfactants,

and in general, surfactant concentration at the field prior to injection for EOR operations. An advantage of our approach is that it can characterize both concentrated systems and low dispersed phase volumes.

Methodology

Acoustic attenuation is a measure of energy lost through sound propagation in media. It can be quantified via acoustic spectroscopy, which measures sound speed and attenuation of ultrasound within a certain frequency range. The advantage of ultrasound is that it can characterize both concentrated systems and low dispersed phase volume where some systems can even be characterized at less than 0.1% vol[11].

Our approach relies on propagating an ultrasound signal through an aqueous solution, measure intrinsic acoustic properties, and determine the solution concentration. The measurements were acquired using an electroacousting spectrometer. A typical setup contains a piezoelectric transducer, which converts an input electrical signal to an ultrasound pulse of a certain frequency and intensity, and then sends it into the sample.

As the pulse passes through the sample and interacts with it, its intensity decreases. Afterwards, a second piezoelectric transducer converts the outputted acoustic pulse back into an electric pulse and sends it to the electronics for comparison with the initial pulse. The attenuation coefficient can be described by Eqn. 1[12]:

$$\alpha = \frac{1}{f\,L} \log \frac{I_{in}}{I_{out}} \qquad 1$$

where α is the attenuation coefficient in dB/cm MHz, f is the frequency in MHz, and L is the gap between the electrodes in cm, I_{in} and I_{out} are the intensity of the received and transmitted signals, respectively.

The decay in intensity is caused by several sources of energy loss. The energy losses include the pulse energy lost in electronics, energy lost due to the limited efficiency in the piezoelectric transducer, and the energy loss that occurs while the ultrasound pulse propagates through the sample and interacts with dispersions[11]. The last energy loss is the target and is extracted from the total energy losses automatically by the instrument.

In this work, the measured acoustic attenuation associated with colloid loss is correlated to the concentrations of the tested surfactants.

Materials

Petroleum sulfonate, Petronate HL/L (51 wt% active ingredient) was purchased from Senneborn. Cocamidopropyl hydroxysultaine (CBS), Cola®Teric CBS was purchased from Colonial Chemical. Synthetic high salinity water was prepared with the following salt compositions/concentrations (g/L): NaCl (41.042), $CaCl_2 \cdot 2H_2O$ (2.385), $MgCl_2 \cdot 6H_2O$ (17.645), Na_2SO_4 (6.343), and $NaHCO_3$ (0.165).

All the listed salts were obtained from Sigma Aldrich.

CBS Solution Preparation

A stock solution of Cola®Teric CBS was diluted into either deionized (DI) water, synthetic high salinity water (S-HSW) or treated high salinity water (T-HSW). 1 g of CBS was weighed and added to 99 mL of DI water, S-HSW, or T-HSW depending on the experiment performed to get 1 wt% CBS solution. A similar process was done to acquire solutions with a final concentration of 0.5 wt%, 1 wt%, 2 wt%, 3 wt%, 4 wt%, and 5 wt%.

Nanosurfactant Preparation

The nanosurfactant formulation was prepared using Petronate HL/L, and CBS as a co-surfactant. High salinity water obtained from a water injection plant was used for the preparation of the nanosurfactant solution. Nanosurfactant solutions were prepared as follows. First, 5 wt% and 4 wt% solutions of the Petronate HL/L and Cola®Teric CBS, respectively, were prepared in DI water[13]. A predetermined ratio based on prior performance optimization experiments was used to mix each solution with high salinity water. The prepared nanosurfactant solutions had a final concentration of 0.2 wt% of active ingredients.

General Procedure Acoustic Attenuation Measurements

Figure 1 is a Dispersion Technology Inc. Acoustic and Electroacoustic spectrometer (DT-1202), which was used for all acoustic attenuation measurements. The instrument was auto-calibrated and used in suspension mode. The sample chamber was thoroughly rinsed with tap water and DI water, and 100 mL of the prepared solutions were poured in the sample chamber while making sure to cover the electrodes. The number of measurements per sample varied depending on the experiment performed with a minimum of three measurements per sample.

Fig. 1 *The Dispersion Technology Inc. Acoustic and Electroacoustic spectrometer (DT-1202) used to perform the attenuation measurements.*

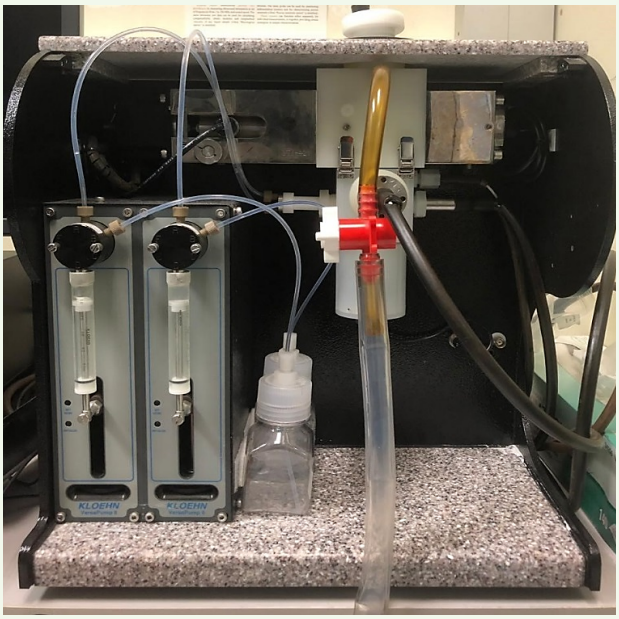

Results and Discussion

We begin by investigating the acoustic attenuation of DI water at different frequencies to establish a baseline. Figure 2 shows the acoustic attenuation of the 100 mL DI water sample, which was measured at frequencies between 3.0 MHz and 99.5 MHz. The experiment was repeated three times by replacing the DI water sample. A total of three different measurements were obtained at each frequency, and the average of these measurements was calculated. The first thing to note is that the variability of the measurements decreases with increasing frequency. Above 55 MHz, the measurements start to converge. A positive relationship between the frequency and attenuation is also observed for frequencies greather than 50 MHz. This is expected because typically higher frequencies experience increased intrinsic attenuation.

Having established our baseline by measuring the intrinsic attenuation of DI water, we proceeded to investigate the effect of CBS — an amphoteric surfactant typically used as a foam booster and viscosity builder — on acoustic attenuation.

Figure 3 shows the acoustic attenuation data obtained from a 100 mL solution of 1 wt% CBS dissolved in DI water. Similar to the DI water spectra, higher frequencies result in less variability of the measurements. In addition, a positive trend between frequency and attenuation is observed. Overall, the attenuation values appeared to be slightly higher than for DI water, suggesting that this approach is sensitive to the presence of CBS and possibly other surfactants. At 99.5 MHz, the average acoustic attenuation of the CBS solution is 0.203 dB/cm/MHz, whereas the DI water solution is 0.195 dB/cm/MHz.

After demonstrating that the presence of CBS in DI water increases the acoustic attenuation, we proceeded to investigate the change in attenuation as a function of the CBS concentration. Acoustic measurements of various concentrations of CBS dissolved in DI water were collected at different frequencies. We limited our measurements to frequencies greater than 65 MHz to reduce the variability of the measurements. The results reveal a positive relationship between acoustic attenuation and CBS concentration, Fig. 4. In agreement with the results previously presented, higher frequencies result in higher attenuation.

By fitting a line to the measured data, it can be seen that the relationship between concentration and attenuation

Fig. 2 *The intrinsic acoustic attenuation of 100 mL of DI water.*

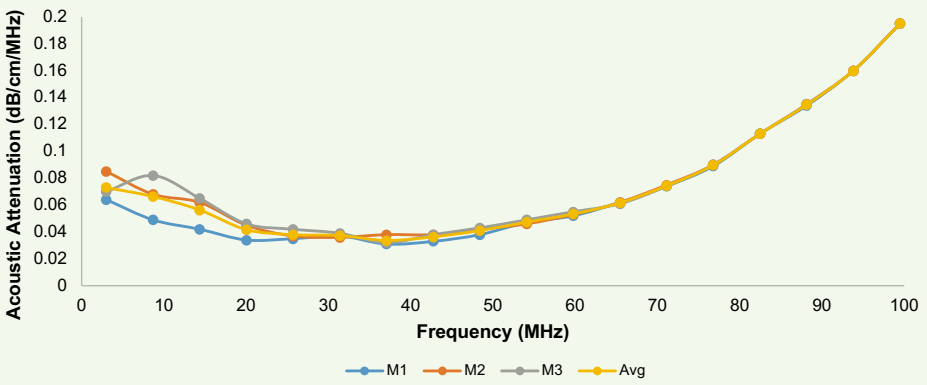

Fig. 3 *The acoustic attenuation of 100 mL of 1 wt% CBS in DI water.*

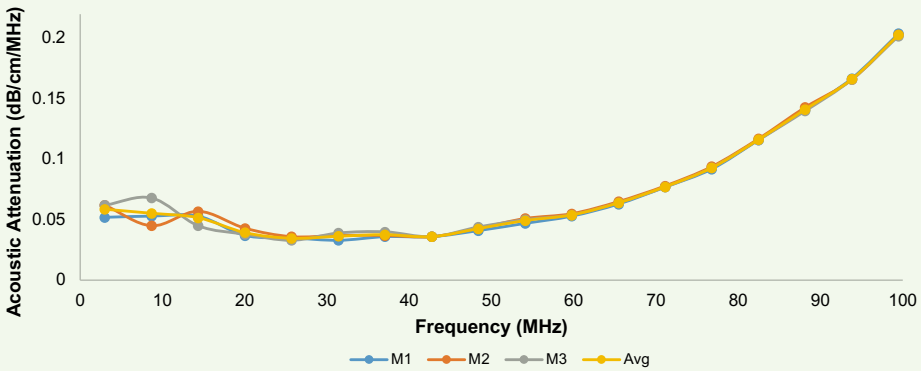

Fig. 4 *The acoustic attenuation of CBS in DI water at several frequencies.*

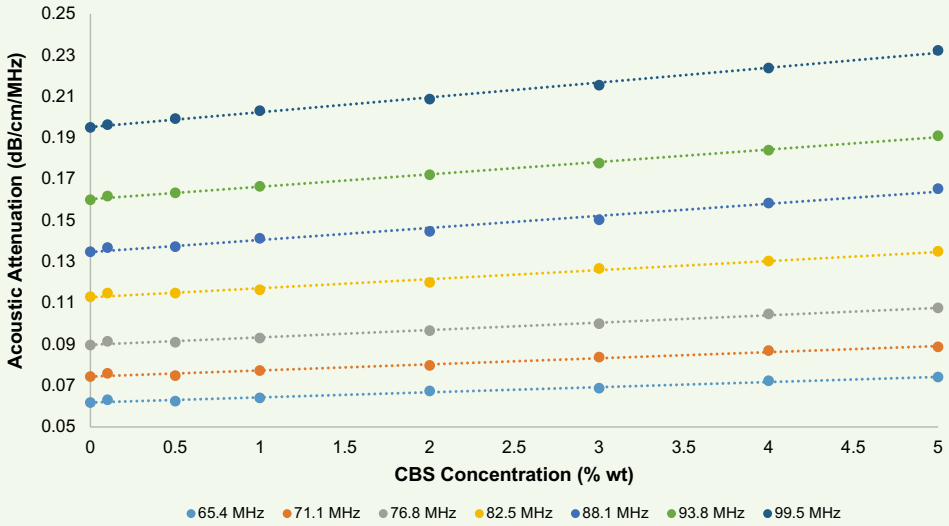

is approximately linear. The R^2 of the linear fit ranges between 0.979 and 0.998, which is a nearly perfect fit of the line to the data.

Table 1 summarizes the measured attenuation at 99.5 MHz for eight different CBS concentrations. A progressive increase in attenuation is observed as the CBS concentration increases. This behavior is expected and can be attributed to the increased particle interactions, which affect the dissipation of the acoustic energy.

Dukhin et al. (2001)[11] previously reported that in the absence of particle-particle interaction, the contribution of the particles to total attenuation is additive. Therefore, it can be concluded that more surfactant molecules present in the solution contribute to the dissipation of the acoustic energy caused by each particle, which causes an increase in the attenuation values.

Our initial tests were all done using DI water as the suspending fluid, however, EOR operations typically involve the use of water with varying amounts of salts dissolved in it. Given that the presence of particles in the solution affects acoustic attenuation, it is important to test if the relationship between acoustic attenuation and the CBS concentration remains distinguishable in other suspending fluids, such as saline water. For this reason, we proceeded to compare CBS solutions in DI water against CBS solutions in synthetic high salinity water (~56,000 ppm TDS), and CBS in saline water obtained from a water injection plant (~56,100 ppm TDS). The acoustic attenuation at 99.5 MHz was measured for the three solutions at different CBS concentrations.

The results, presented in Fig. 5, display the previously observed trend of attenuation being a linear function of the surfactant concentration. It can also be seen that attenuation increases with salinity. At a constant CBS concentration, the acoustic attenuation in DI water is less than the S-HSW, which is less than the acoustic attenuation in the T-HSW.

Saline water, displaying greater attenuation values than DI water, can be attributed to the structured water layers around ions formed as a result of the interaction of the ion's electric charges with water molecules' dipole moment[12]. Viscoelastic properties of water in these layers are different compared to bulk. Sound speed goes up with ionic strength because of the orientation of water molecules in the ion's solvating layers. This increases the elasticity of the water.

Subsequently, we were surprised by the attenuation difference between S-HSW and T-HSW, even though their salinities are almost identical. This could possibly be attributed to the presence of additional impurities in T-HSW, thereby further modifying the water layers. Upon further investigation, we noticed that the temperature of the DI water and saline water was slightly different (< 1 °C). We suspected that temperature could have played an

Table 1 *The acoustic attenuation at 99.5 MHz for several concentrations of CBS solution in DI water.*

	CBS Concentration (wt%)							
	0	0.1	0.5	1	2	3	4	5
Attenuation (dB/cm/MHz)	0.195	0.196	0.199	0.203	0.209	0.215	0.224	0.232

Fig. 5 *The acoustic attenuation of CBS in three different suspending fluids.*

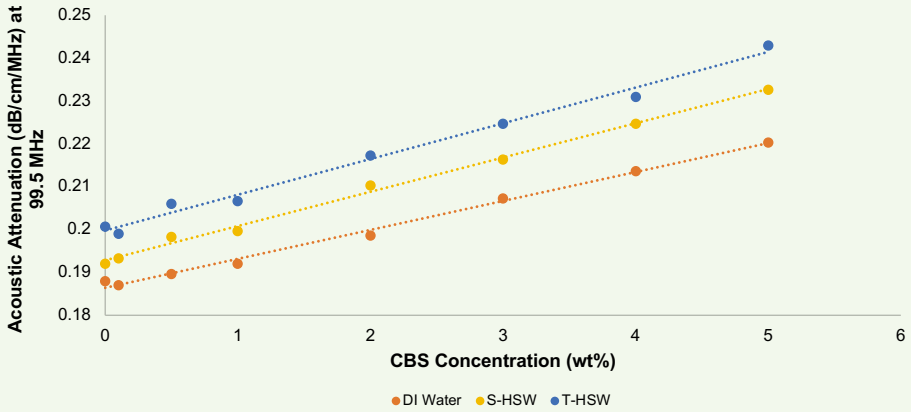

additional role in the change in attenuation. Ultrasound interactions within dispersed systems include a thermal mechanism, which is related to the temperature gradients generated near the particle surface. The dissipation of acoustic energy caused by thermal losses is actually the dominant attenuation effect for soft particles such as emulsion droplets[12].

We performed additional tests to assess the sensitivity of our process to temperature variations. Solutions of various CBS concentrations were heated to 35 °C, then measured for acoustic attenuation while naturally cooling down to approximately 27 °C.

Figure 6 shows the results obtained from these measurements. Our previously established trend with concentration appears to be sustainable throughout the entire temperature range of 27 °C to 35 °C, even with the overall reduction of attenuation resulting from the increase in solution temperature. The sustainability of the attenuation behavior regardless of slight temperature fluctuations supports our process' suitability for field application.

Additionally, we examined the effect of smaller temperature fluctuations on the attenuation at temperatures approximately between 25 °C and 27 °C. Figure 7 shows the attenuation spectra obtained where the same behavior is seen where higher temperature measurements correspond to slightly lower attenuation values, even at constant concentration.

It appears that the attenuation of very low concentrations (< 1 wt%) is more affected by the temperature fluctuation as opposed to the higher concentrations (> 1 wt%). This could be a challenge for highly dispersed solutions because our approach would require a good control of the sample temperature. Although, solutions with a surfactant concentration greater than 1 wt% would experience a much lower temperature effect.

We then attempted to correct the obtained attenuation values at a different temperature to a fixed temperature value we set at 24 °C. We established a temperature correction factor based on the slope of the 1 wt% CBS solution, Fig. 8. It can be noticed that the attenuation offset is slightly reduced after the temperature correction step.

Table 2 shows the attenuation values before and after

Fig. 6 *The acoustic attenuation at temperatures between 27 °C and 35 °C for several concentrations of the CBS solution in DI water.*

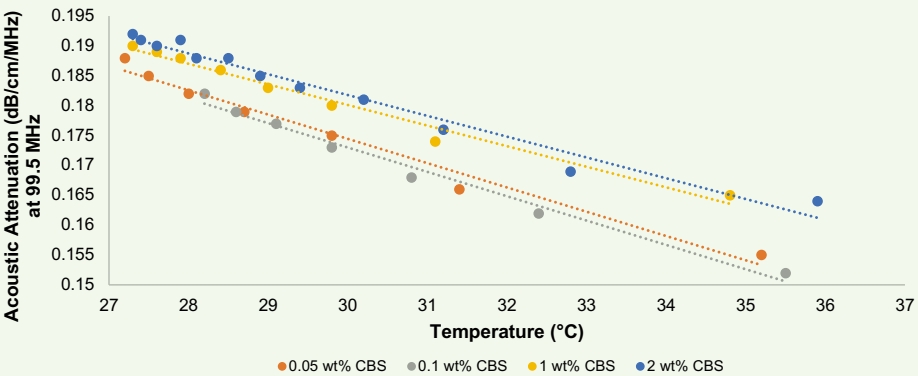

Fig. 7 *The acoustic attenuation at temperatures between 25 °C and 27 °C for several concentrations of the CBS solution in DI water.*

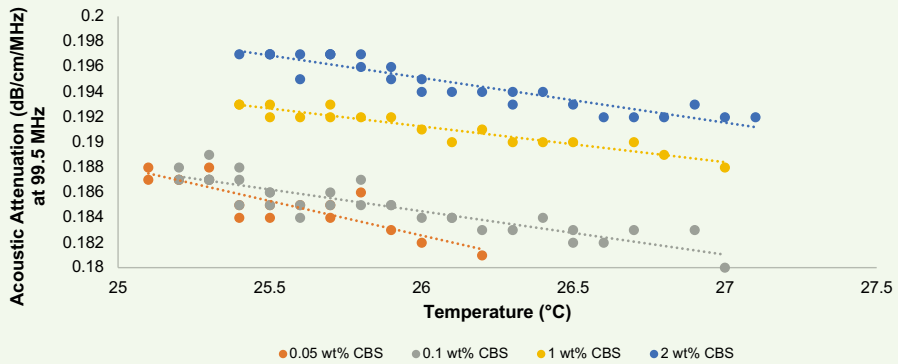

Fig. 8 *The corrected attenuation values of the 1 wt% CBS in DI water.*

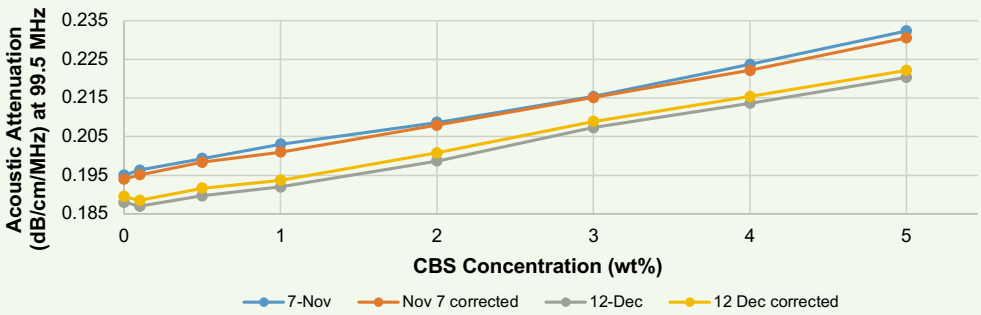

temperature correction, along with the final difference in attenuation. After correction, the difference in attenuation for all tested concentrations is < 0.01 db/cm/MHz, which is the claimed instrument precision.

After establishing the relationship between the acoustic attenuation and the surfactant concentration using CBS we proceeded to measure the acoustic attenuation of our nanosurfactant. Figure 9 shows the acoustic attenuation spectra obtained for several concentrations of nanosurfactant in the frequency range of 65 MHz to 99.5

Table 2 *The attenuation values of the CBS solutions in DI water before and after temperature correction.*

CBS Concentration (wt%)	Nov. 7	Nov. 7 Corrected	Dec. 12	Dec. 12 Corrected	Δα
0	0.195	0.194	0.188	0.1895	-0.0045
0.1	0.196333	0.195133333	0.187	0.1885	-0.0066
0.5	0.199333	0.198333333	0.189667	0.191666667	-0.0066
1	0.203	0.201	0.192	0.1937	-0.0073
2	0.208667	0.207966667	0.198667	0.200766667	-0.0072
3	0.215333	0.215133333	0.207333	0.208933333	-0.0062
4	0.223667	0.222166667	0.213667	0.215366667	-0.0068
5	0.232333	0.230533333	0.220333	0.222133333	-0.0084

Fig. 9 *The acoustic attenuation obtained for several concentrations of nanosurfactant in the frequency range of 65 MHz to 99.5 MHz.*

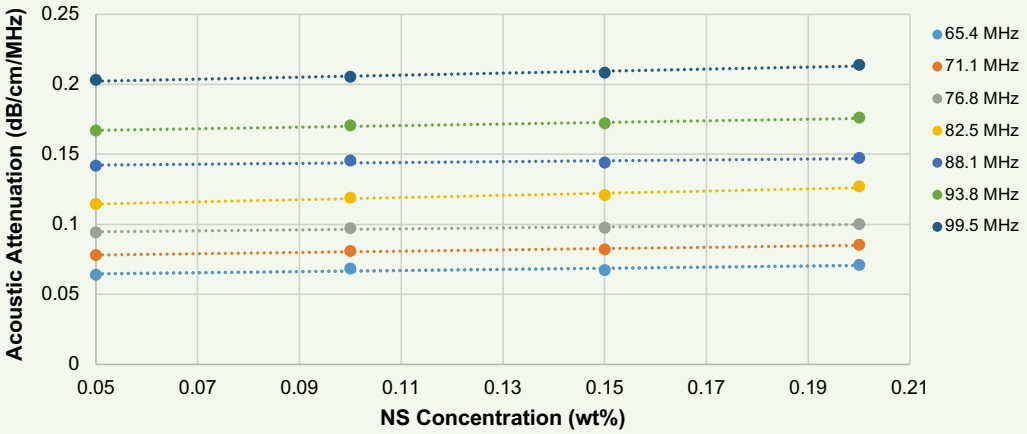

MHz. We noticed the same trend seen previously using CBS where attenuation is dependent on the surfactant concentration. The R^2 values shown on the plot for our linear fit of several frequencies appear between 0.796 and 0.969, indicating a close fit of the line to the data.

Having developed attenuation calibration curves, such as the one presented here, the last step in our approach is to collect a sample of the injection fluid and measure its acoustic attenuation. By comparing the obtained value against the calibration curve, it would be possible to establish its concentration. This process takes only a few minutes and requires minimum preparation.

Summary and Conclusions

We have demonstrated that acoustic attenuation changes, as a function of surfactant concentration, specifically CBS and nanosurfactant, in various solutions. While attenuation can be measured at different frequencies, our results show that for a range between 3.0 MHz to 99.5 MHz, higher frequencies yield measurements with less variability, and therefore, we recommend measuring attenuation at frequencies greater than 60 MHz. Salinity and temperature have a significant effect on acoustic attenuation.

The salinity effect can be accounted for by developing calibration curves using the same suspending fluid intended for the EOR operations. The results show that even slight variations in salinity and/or composition can cause significant changes in attenuation. Therefore, special attention must be paid to the composition of the suspending fluid when conducting laboratory experiments to develop the concentration calibration curves.

To account for temperature variations, a correction factor can be estimated by measuring the attenuation of a given concentration at different temperatures. This factor can be used to estimate the attenuation at a common temperature for different measurements. As a whole, the results presented in this work prove that acoustic spectroscopy is a useful method for use in the field to aid EOR operations by providing reliable in situ concentration measurements of surfactant solutions.

Acknowledgments

This article was prepared for presentation at the Abu Dhabi International Petroleum Exhibition and Conference, Abu Dhabi, UAE, November 9-12, 2020.

The authors would like to thank the following indivduals: Dr. Afnan Mashat, for her support in preparing the nanosurfactant samples, and Fouad Sadis, for his support in conducting the acoustic experiments.

References

1. Babadagli, T.: "Philosophy of EOR," *Journal of Petroleum Science and Engineering*, Vol. 188, May 2020.
2. Hirasaki, G.J., Miller, C.A. and Puerto, M.: "Recent Advances in Surfactant EOR," SPE paper 115386, presented at the SPE Annual Technical Conference and Exhibition, Denver, Colorado, September 21-24, 2008.
3. Sirdesai M. and Khilar, K.C.: "A Model for Microencapsulation in Polyurea Shell by Means of Interfacial Polycodensation," *The Canadian Journal of Chemical Engineering*, Vol. 66, Issue 3, June 1988, pp. 509-513.
4. Hirasaki, G.J., Miller, C.A. and Puerto, M.: "Recent Advances in Surfactant EOR," *SPE Journal*, Vol. 16, Issue 4, July 2011, pp. 889-907.
5. Han, M., AlSofi, A., Fuseni, A., Zhou, X., et al.: "Development of Chemical EOR Formulations for a High Temperature and High Salinity Carbonate Reservoir," IPTC paper 17084, presented at the International Petroleum Technology Conference, Beijing, China, March 26-28, 2013.
6. Kamal, M.S., Sultan, A., Hussein, I., Hussain, S.M., et al.: "Screening of Surfactants and Polymers for High Temperature High Salinity Carbonate Reservoirs," SPE paper 192441, presented at the SPE Kingdom of Saudi Arabia Annual Technical Symposium and Exhibition, Dammam, Saudi Arabia, April 23-26, 2018.
7. Zulkifli, N.N., Mahmood, S.M., Akbari, S., Manap, A.A., et al.: "Evaluation of New Surfactants for Enhanced Oil Recovery Applications in High-Temperature Reservoirs," *Journal of Petroleum Exploration and Production Technology*, Vol. 10, June 2019, pp. 283-296.

8. Wellington, S.L. and Richardson, E.A.: "Low Surfactant Concentration Enhanced Waterflooding," *SPE Journal*, Vol. 2, Issue 4, December 1997, pp. 389-405.

9. Abdel-Fattah, A.I., Mashat, A., Alaskar, M. and Gizzatov, A.: "NanoSurfactant for EOR in Carbonate Reservoirs," SPE paper 188046, presented at the SPE Kingdom of Saudi Arabia Annual Technical Symposium and Exhibition, Dammam, Saudi Arabia, April 24-27, 2017.

10. Mashat, A., Abdel-Fattah, A.I. and Gizzatov, A.: "NanoSurfactant: A Novel Nanoparticle-Based EOR Approach," SPE paper 190861, presented at the SPE EUROPEC featured at the 80th EAGE Conference and Exhibition, Copenhagen, Denmark, June 11-14, 2018.

11. Dukhin, A.S. and Goetz, P.J.: "Acoustic and Electroacoustic Spectroscopy for Characterizing Concentrated Dispersions and Emulsions," *Advances in Colloid and Interface Science*, Vol. 92, Issues 1-3, September 2001, pp. 73-132.

12. Dukhin, A.S. and Goetz, P.J.: "Electrokinetics at High Ionic Strength and Hypothesis of the Double Layer with Zero Surface Charge," *Langmuir*, Vol. 21, July 2005, pp. 9990-9997.

13. Gizzatov, A., Mashat, A., Kosynkin, D., Alhazza, N., et al.: "Nanofluid of Petroleum Sulfonate Nanocapsules for Enhanced Oil Recovery in High Temperature and High Salinity Reservoirs," *Energy Fuels*, Vol. 33, Issue 11, pp. 11567-11573.

About the Authors

Hala A. AlSadeg

B.S. in Materials Science and Engineering, Pennsylvania State University

Hala A. AlSadeg is a Petroleum Scientist working with the Reservoir Engineering Technology Team of Saudi Aramco's Exploration and Petroleum Engineering Center – Advanced Research Center (EXPEC ARC). She works on several research projects aimed at utilizing nanotechnology for enhanced oil recovery and reservoir characterization applications.

In 2018, Hala received her B.S. degree (highest honors) in Materials Science and Engineering from the Pennsylvania State University, State College, PA. Her undergraduate research was focused on the fabrication and characterization of 2D heterostructures for sensing and electronic applications.

Jesus M. Felix Servin

M.S. in Chemical and Biological Engineering, King Abdullah University of Science and Technology

Jesus M. Felix Servin joined the Reservoir Engineering Technology Division of Saudi Aramco's Exploration and Petroleum Engineering Center – Advanced Research Center (EXPEC ARC) in February 2012. His focus is on the development of electromagnetic methods and nanoparticle-based contrast agents for reservoir characterization and monitoring. Jesus's role has been instrumental in the development and deployment of the Magnetic Nano-Mappers project, including hardware design and in-house fabrication, instrumentation, computer programming, and data processing.

Jesus' interests include the development of nanoscale strategies for reservoir illumination and electromagnetic methods for reservoir description and monitoring.

He received his B.S. degree in Engineering Physics from Instituto Tecnologico y de Estudios Superiores de Monterrey, Monterrey, Mexico, and an M.S. degree in Chemical and Biological Engineering from King Abdullah University of Science and Technology, Thuwal, Saudi Arabia.

Dr. Amr I. Abdel-Fattah

Ph.D. in Chemical Engineering, University of New Mexico

Dr. Amr I. Abdel-Fattah is a Petroleum Engineering Specialist and Team Leader of the In-Situ Sensing and Intervention focus area in Saudi Aramco's Exploration and Petroleum Engineering Center – Advanced Research Center (EXPEC ARC). He joined EXPEC ARC's Reservoir Engineering Technology Division in late 2012 after working 16 years with the Los Alamos National Laboratory in New Mexico, U.S., where he reached a Senior Scientist status. Amr is currently spearheading a number of research and technology development programs in EXPEC ARC geared at utilizing nanotechnology for upstream oil and gas applications.

He has over 30 years of experience in subsurface energy and environmental applications of nanotechnology, colloid and interface science, and electrokinetics. Amr is a Society of Petroleum Engineers (SPE) Distinguished Lecturer, a founding Board Member of the International Association of Electrokinetics, a U.S. Representative on the International Board of Electrokinetics, a Technical Member on the Science Advisory Board of the International Association of Colloid and Interface Scientists, and a Guest Editor for the international *Journal of Colloids and Surfaces A*.

He has published numerous papers in international journals, including some of the world's premier and most cited journals, and delivered numerous plenary and invited talks and lectures worldwide. Amr chaired the International Electrokinetics Conference in Santa Fe, NM, in 2008, in addition to several international workshops and conference sessions in the U.S., Canada, and Europe since 2005.

He received his B.S. degree in Civil Engineering and an M.Eng. in Geotechnical Engineering from Ain Shams University, Cairo, Egypt. Amr received his M.S. degree and his Ph.D. degree in Chemical and Nuclear Engineering from the University of New Mexico, Albuquerque, NM.

Development of Oriented Fracturing of Chemically Induced Pressure Pulse for Unconventional Gas Reservoirs

Ayman R. Al-Nakhli

Abstract /

Commercial production from unconventional reservoirs require new technologies to reduce the breakeven cost. Multistage fracturing was an enabler of gas production from such reservoirs; however, it is responsible for significant cost. Fracturing jobs cancelation, due to high pressure, results in nonproductive wells, which also represent high cost. Unfractured wells results in locked and unproduced potential gas.

One of the major challenges that is faced by fracturing companies is the high breakdown pressure of such reservoirs, which exceeds tubular and pumping pressure limitations. This results in nonfractured wells. A recently developed technology is a chemically induced pressure pulse, where exothermic reaction is triggered in situ to generate a pressure pulse sufficient to fracture the formation. Initiated fractures are then propagated with hydraulic fracturing. This article is a study on the generated fractures, using a chemical pulse, on confined and unconfined conditions. The study shows a successful new technique of orienting the pulse fracturing.

The objective of developing a new method of orienting the in situ pressure pulse is to increase the stimulated reservoir volume in unconventional reservoirs, and ultimately enhancing commercial production. The technology will also enable the fracturing of high-stress rocks, deep unconventional reservoirs, as conventional hydraulic fracturing method fails to fracture the formation.

A novel technique for oriented chemically pulse fracturing was developed. The invented method is to create oriented fractures around the wellbore, and therefore enhance productivity. Having an oriented chemical pulse fracturing will significantly impact the application of this technology for unconventional gas, especially during long horizontal wells.

Introduction

Tight and unconventional gas are located in very competent rocks, which results in significant fracturing cancellation due to high breakdown pressure[1-3]. Enabling the fracturing of such reservoirs by reducing the breakdown pressure will not only reduce the cost of drilling new wells, but also increase gas production. Reducing the costs will also promote commercial production from unconventional reservoirs.

High breakdown pressure could be due to low permeability, a high Young's modulus of the rock or low-pressure rating of the well completion[4-6]. Filter cake sometimes plays a major factor to increase the breakdown pressure.

There are three types of fracturing: explosives, tailored pulse loading, and hydraulic fracturing, Fig. 1. Technically, when the fracturing pressurization rate is fast, multiple fractures are expected. When the pressurization rate is slow, a single fracture should be created. For these three fracturing types, the pressurization rate for explosives is in micro-seconds ($P \geq 107$ MPa), so multiple fractures are created. A compacted zone is created around the wellbore, which will have low permeability and impair production. Pulse loading, using a gas gun, also creates multiple fractures without a damaged zone around the wellbore, as the pressurization rate is in milliseconds, $p \approx 102 \sim 106$ MPa/s. Hydraulic fracturing creates a single bi-wing fracture as the pressurization rate in minutes, $P \leq 1$ MPa/s[7-9].

Chemically Induced Pulse Fracturing

A novel method, based on a chemically in situ pressure pulse, was developed. The technology describes generating an in situ pressure pulse, using a thermochemical fluid, to initiate the fracture and to be propagated with hydraulic pressure. The pressure pulse was measured in the lab, in a contained reactor environment, up to 20,000 psi. Generating a higher pressure pulse was avoided for safety reasons.

Figure 2 shows reactor testing of the pressure pulses, generated by thermochemical reaction. The initial pressure was at zero, and reached up to 16,650 psi due to a reaction, and the reactor temperature increased up to 275 °F.

Fig. 1 *Three types of fracturing[7].*

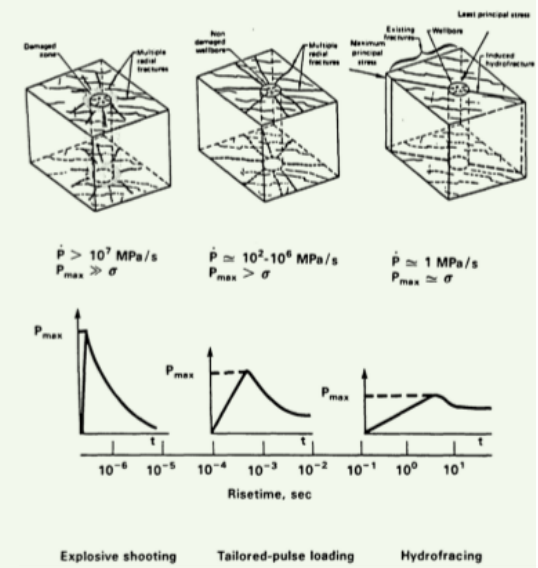

Fig. 2 *Reactor testing of in situ pressure pulses generated using thermochemical fluid.*

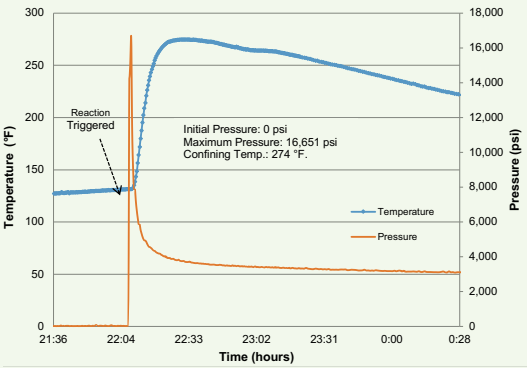

Fig. 3 *The HPHT autoclave system, rated up to 20,000 psi and 500 °C.*

Experimental Work

Autoclave Testing

A high-pressure, high temperature (HPHT) autoclave system was used to study the kinetics of the exothermic reaction, Fig. 3. The system is rated up to 20,000 psi and 500 °C. Experiments were carried out in a dedicated specialized HPHT laboratory, equipped with the required safety features. The experimental parameters were controlled and monitored remotely via a PC.

Results of the real-time pressure and temperature data are recorded every 2 seconds during the chemical reaction. This testing phase is performed to measure pressure and temperature profiles of the exothermic reactions at downhole conditions[10].

Biaxial Frame Testing

A series of laboratory experiments were conducted to provide insight on applying the concept of chemically induced pulsed fracturing in the field. Cement samples used in these experiments were rectangular blocks with dimensions of 8" × 8" × 8", for confined testing using a biaxial frame, Fig. 4. For unconfined pulse testing, a regular coreflood system was used with 10" × 10" × 10" cement samples.

The man-made rock samples were cast from mixing water and cement with a weight ratio of 31/100, respectively. For the unconfining testing, each rock sample was made to have a cavity of 1½" × 3", to simulate a wellbore, Fig. 5a. For the confined test, the vertical open hole was cast all the way in the center of the block, Fig. 5b.

The physical and mechanical properties of the rock samples are: porosity = 29%, bulk density = 1.82 gm/cc, Young's modulus = 1.92 × 106 psi, Poisson's ratio = 0.26, uniaxial compressive strength = 3,299 psi, cohesive strength = 988 psi, and the internal friction angle = 28°.

The breakdown pressure for this test was 5,400 psi. The exothermic chemicals were used with slick water. The concentrations of the exothermic chemicals varies from 3 to 5 molar and were used immediately after preparation. The injection rate was about 30 cc/min to 100 cc/min.

The samples were tested with and without confinement. For the confined stress testing, samples were loaded in a biaxial cell with equal horizontal stress of 2,000 psi for one test, and 5,000 psi for another test. If we consider a depth of 2,570 ft, these stress levels represent gradients of 0.78 psi/ft, and 1.56 psi/ft, respectively. The reactive

Fig. 4 *The biaxial system used for the testing.*

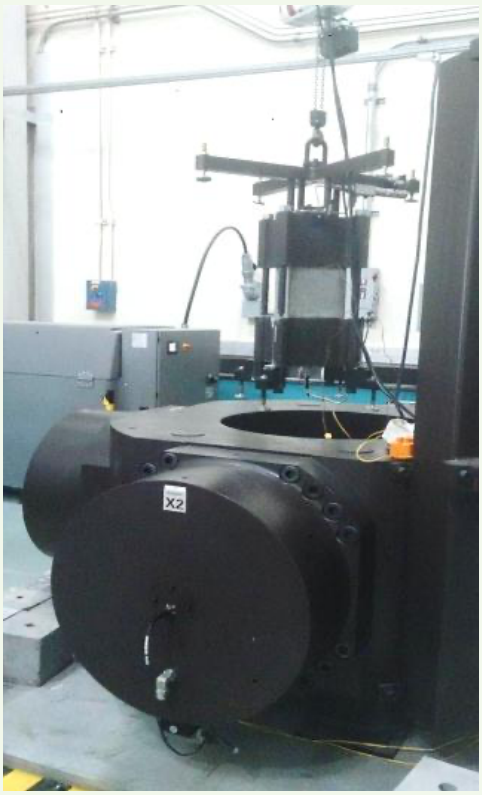

Fig. 5 *(a) The block design for the unconfined tests, and (b) The block design for the confined tests.*

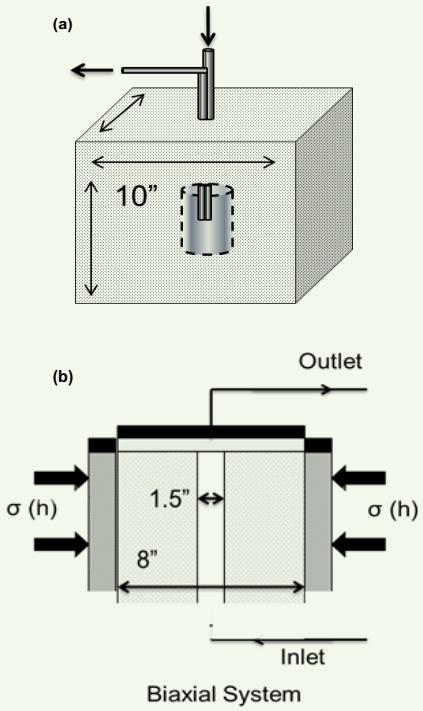

chemicals were injected in the block and heat was applied using the biaxial plates.

Unconfined Testing (without Casing)

The samples of this type of test, which simulate an open hole vertical well, were man-made cement blocks. The rock samples were preheated to 200 °F. Then, reactive chemicals were injected in the rock at atmospheric pressure at a rate of 15 cc/min. Once the chemical injection was complete and the reaction took place, multiple fractures were created, Figs. 6a and 6b.

The created fractures were longitudinal and perpendicular in respect to the vertical wellbore. The fracture geometry indicates that fractures propagated from the wellbore to the end of the sample. This indicates that the pressure generated was greater than compressive strengths of the samples. The breakdown pressure for this test was 5,400 psi.

Unconfined Testing (with Pre-Perforated Casing and Notches)

Pre-perforated casing was used with the cement block for the pulse test, where similar procedures were followed as previously described. We found that the pre-perforated casing had oriented the created fracture into one single bi-wing fracture. Figure 7a is the perforated casing. Two perforations where placed on each side of the casing.

Figures 7b and 7c shows the cement block after the pulse test with a single bi-wing fracture. Another test was conducted, where the cement block used had four notches, simulating an open hole wellbore. The same results were achieved with a single bi-wing fracture, Fig. 8.

Confined Testing (without Casing)

Samples of this testing simulates a vertical and open hole well drilled in the center of an 8” × 8” × 8” cube, Fig. 9. The wellbore is 1.5” in diameter, extending throughout the whole length of the sample, as previously shown in Fig. 5b.

The tested sample was then placed in a biaxial loading frame where two horizontal stress levels of a given stress were applied, while the vertical stress was controlled by mechanical tightening of the base and top platens. Then, reactive chemicals were injected into the rock at

Fig. 6 *(a) Pretreatment; and (b) post-treatment of the portrait cement block sample, using chemically pulsed fracturing.*

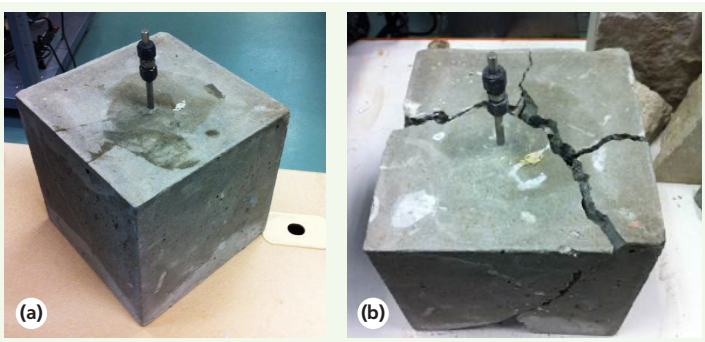

Fig. 7 *(a) The pre-perforated casing, (b) and (c) post-reaction pulse of the portrait cement block sample.*

Fig. 8 *Chemically pulsed fracturing in a cement block with four notches, simulating an open hole wellbore.*

atmospheric pressure and room temperature at a rate of 15 cc/min. The sample was then heated for 2 to 3 hours until the reaction took place and fractures were created. Two tests were performed as follows.

During this test, the applied horizontal stress level was 4,000 psi in both directions, Fig. 9. The reaction was triggered at 167 °F. Upon triggering the reaction, four longitudinal fractures were created with respect to the vertical hole, Figs. 10a. 10b, and 10c. The fracture geometry shows that the created fracture was longitudinal in respect to the vertical wellbore. This indicates that the pressure generated was greater than 8,000 psi. Each created planar fracture propagated in the direction of one σH, and perpendicular to the direction of the other σH, as the applied stress is equal in both horizontal directions.

Fig. 9 *The biaxial frame test of pulsed fracturing under 4,000 psi of confined stress for the open hole cement block.*

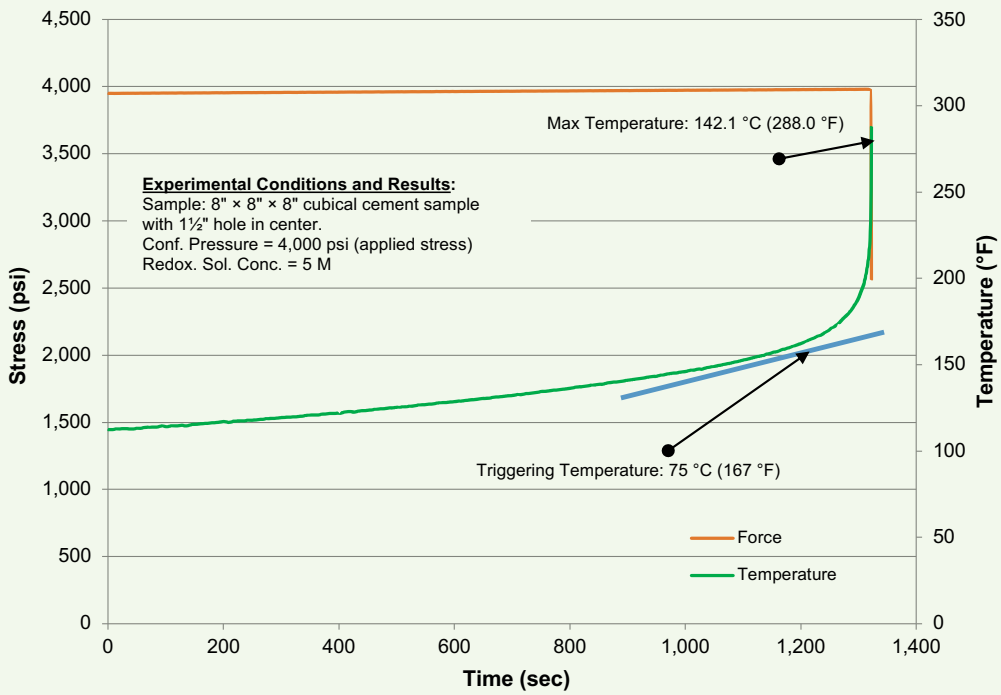

Fig. 10 *(a) The open hole 8" × 8" × 8" cement block, (b) and (c) pre- and post-test in the biaxial frame under 4,000 psi of stress, respectively.*

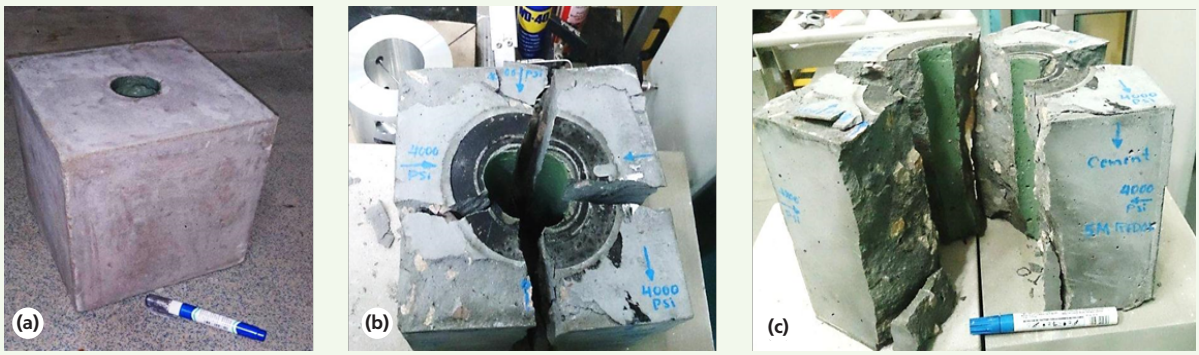

Confined Testing (with Casing)

During this test, the applied horizontal stress level was 5,000 psi at both directions, Fig. 11. For this test, a pre-perforated casing was used in the cement sample identical to the previous test using the biaxial frame described earlier. The cement sample had a cased hole in the center of the 8" × 8" × 8" block, Fig. 12a. The wellbore is 1½" in diameter extending throughout the whole length of the sample.

The reaction was triggered at 144 °F. Upon triggering the reaction, bi-wing longitudinal fractures were created with respect to the vertical hole, Fig. 12b. The fracture geometry shows that the created fracture was longitudinal in respect to the vertical wellbore. This indicates that the pressure generated was greater than 10,000 psi.

Discussion

Pulse fracturing creates multiple fractures when the pressurization rate is in milliseconds, p ≈ 102 ~ 106 MPa/s, as shown in current and previous studies. During the unconfined pulse testing using thermochemical fluid, multiple fractures were created. Three main vertical fractures were randomly created along the wellbore. A secondary fourth fracture was created as an extension of one of the primary fractures. So, several random fractures were created as a result of chemically pulse fracturing in an open hole cement block.

Another type of testing was conducted using a

Fig. 11 *The biaxial frame test of the pulsed fracturing under 5,000 psi of confined stress for the cased hole cement block.*

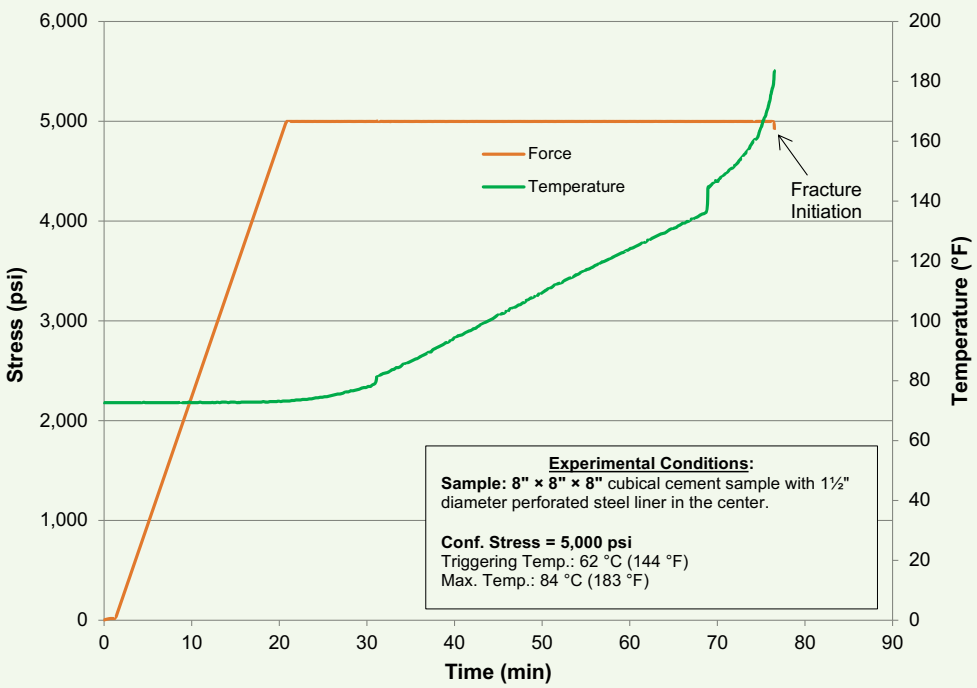

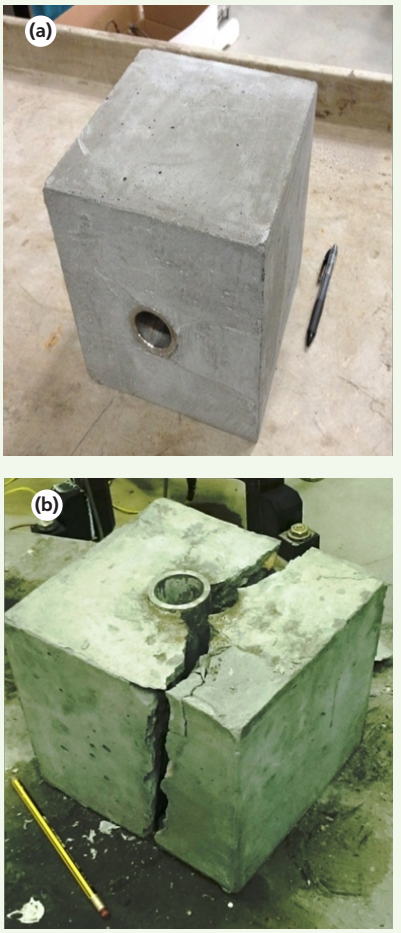

Fig. 12 *(a) The cement sample with a cased hole in the center of the 8″ × 8″ × 8″ block. (b) The same block post-test after 5,000 psi of stress was applied in both directions.*

pre-perforated casing, using the same testing procedures. An oriented bi-wing fracture was created. This shows that a perforated casing will orient random multiple fractures into one single fracture. This will help not only to focus the pulse wave energy, but also will selectively place the fracture in downhole conditions. In another test conducted, notches were also found to orient the pulse fractures, in open hole wells, as the perforated casing do.

For confining testing, a biaxial frame was used to apply stress on the cement block during pulse testing. In one test, 4,000 psi of stress was equally applied, in both horizontal directions, on a cement block with an open hole wellbore. As a result, four vertical and random fractures were created in the cement block. The pressure pulse created by the exothermic reaction exceeded the stress cage of 8,000 psi around the wellbore.

A cement block, with a pre-perforated casing, was used for another pulse test. The biaxial frame was used to apply 5,000 psi of stress in both horizontal directions. For this test, a single bi-wing fracture was created. This shows that the pre-perforated casing had also oriented the created fractures into one single fracture.

Conclusions

In this study, pulse fracturing testing was conducted on cement blocks, with confined and unconfined conditions. Based on the results achieved, the following conclusions can be drawn:

1. A novel fracturing method was developed using thermochemical reaction. Application of a thermochemical reaction can create pressure pulse sufficient to fracture cement blocks.
2. The chemically induced pulse created random and multiple fractures in cement blocks with an open hole wellbore. The same results are achieved with unconfined and confined testing.
3. Successfully, pulse fracturing was oriented using a pre-perforated casing, with confined and unconfined conditions. A single bi-wing fracture was created.
4. Cement blocks, with open hole wellbore and notches, were also tested using pulse fracturing. The created notches had successfully oriented the fractures into a single bi-wing fracture.
5. Both the pre-perforated casing and notches had shown a successful orientation of chemically pulse fracturing, and created a single bi-wing fracture.

Acknowledgments

This article was prepared for presentation at the Abu Dhabi International Petroleum Exhibition and Conference, Abu Dhabi, UAE, November 9-12, 2020.

References

1. Al-Nakhli, A.R., BaTaweel, M., Mustafa, A., Tariq, Z., et al.: "Novel Methodology to Reduce the Strength of High Stress-Tight Gas Reservoirs Using Thermochemical," paper presented at the 53rd U.S. Rock Mechanics/Geomechanics Symposium, New York City, New York, June 23-26, 2019.
2. Al-Nakhli, A.R., Abass, H., Kwak, H.T., Al-Badairy, H., et al.: "Overcoming Unconventional Gas Challenges by Creating Synthetic Sweetspot and Increasing Drainage Area," SPE paper 164165, presented at the SPE Middle East Oil and Gas Show and Conference, Manama, Kingdom of Bahrain, March 10-13, 2013.
3. Barree, R.D., Gilbert, J.V. and Conway, M.: "Stress and Rock Property Profiling for Unconventional Reservoir Stimulation," SPE paper 118703, presented at the SPE Hydraulic Fracturing Technology Conference, The Woodlands, Texas, January 19-21, 2009.
4. Beugelsdijk, L.J.L., de Pater, C.J. and Sato, K.: "Experimental Hydraulic Fracture Propagation in a Multi-Fractured Medium," SPE paper 59419, presented at the SPE Asia Pacific Conference on Integrated Modeling for Asset Management, Yokohama, Japan, April 25-26, 2000.
5. Britt, L.K., Hager, C.J. and Thompson, J.W.: "Hydraulic Fracturing in a Naturally Fractured Reservoir," SPE paper 28717, presented at the International Petroleum Conference and Exhibition of Mexico, Veracruz, Mexico, October 10-13, 1994.
6. Chu, T.Y., Jacobson, R.D., Warpiniski, N. and Mohaupt, H.: "Geothermal Well Stimulation Using High Energy Gas Fracturing," in *Proceedings of the 12th Workshop on Geothermal Reservoir Engineering*, January 1987, pp. 279-284.

7. Schatz, J.F., Zeigler, B.J., Hanson, J.M., Christianson, M.C., et al.: "Laboratory, Computer Modeling, and Field Studies of the Pulse Fracturing Process," SPE paper 18866, presented at the SPE Production Operations Symposium, Oklahoma City, Oklahoma, March 13-14, 1989.

8. Cho, S.H. and Kaneko, K.: "Influence of the Applied Pressure Waveform on the Dynamic Fracture Processes in Rock," *International Journal of Rock Mechanics and Mining Sciences*, Vol. 41, Issue 5, July 2004, pp. 771-784.

9. Cuderman, J.F.: "Multiple Fracturing Experiments — Propellant and Borehole Considerations," SPE paper 10845, presented at the SPE/DOE Unconventional Gas Recovery Symposium, Pittsburgh, Pennsylvania, May 16-18, 1982.

10. Al-Nakhli, A.R.: "Chemically Induced Pressure Pulse to Increase Simulated Reservoir Volume in Unconventional Reservoirs," URTEC paper 1922369, presented at the SPE/AAPG/SEG Unconventional Resources Technology Conference, Denver, Colorado, August 25-27, 2014.

About the Author

Ayman R. Al-Nakhli

M.S. in Entrepreneurship for New Business Development, Open University Malaysia

Ayman R. Al-Nakhli is a Petroleum Scientist in Saudi Aramco's Exploration and Petroleum Engineering Center – Advanced Research Center (EXPEC ARC), where he leads the research program on thermochemicals and develops technologies related to conventional and unconventional reservoirs such as pulse fracturing, stimulation, diverting agents, and heavy oil.

Ayman has developed and field deployed several novel technologies, with four of them being commercialized with international service companies. He received the World Oil Award for Best Production Chemical in 2015.

Ayman has filed more than 20 patents, published 35 journal papers, and 40 conference papers.

He received his B.S. degree in Industrial Chemistry from King Fahd University of Petroleum and Minerals (KFUPM), Dhahran, Saudi Arabia, and an M.S. degree in Entrepreneurship for New Business Development from Open University Malaysia, Bahrain.